

The diffuse Nitsche method: Dirichlet constraints on phase-field boundaries

Lam H. Nguyen¹, Stein K.F. Stoter¹, Martin Ruess²,
Manuel A. Sanchez Uribe³, Dominik Schillinger^{1,*}

¹*Department of Civil, Environmental, and Geo-Engineering, University of Minnesota, Twin Cities, USA*

²*School of Engineering, University of Glasgow, United Kingdom*

³*School of Mathematics, University of Minnesota, Twin Cities, USA*

SUMMARY

We explore diffuse formulations of Nitsche's method for consistently imposing Dirichlet boundary conditions on phase-field approximations of sharp domains. Leveraging the properties of the phase-field gradient, we derive the variational formulation of the diffuse Nitsche method by transferring all integrals associated with the Dirichlet boundary from a geometrically sharp surface format in the standard Nitsche method to a geometrically diffuse volumetric format. We also derive conditions for the stability of the discrete system and formulate a diffuse local eigenvalue problem, from which the stabilization parameter can be estimated automatically in each element. We advertise metastable phase-field solutions of the Allen-Cahn problem for transferring complex imaging data into diffuse geometric models. In particular, we discuss the use of mixed meshes, that is, an adaptively refined mesh for the phase-field in the diffuse boundary region and a uniform mesh for the representation of the physics-based solution fields. We illustrate accuracy and convergence properties of the diffuse Nitsche method and demonstrate its advantages over diffuse penalty-type methods. In the context of imaging based analysis, we show that the diffuse Nitsche method achieves the same accuracy as the standard Nitsche method with sharp surfaces, if the inherent length scales, i.e., the interface width of the phase-field, the voxel spacing and the mesh size, are properly related. We demonstrate the flexibility of the new method by analyzing stresses in a human vertebral body.

Copyright © 2000 John Wiley & Sons, Ltd.

KEY WORDS: The diffuse Nitsche method; diffuse domain methods; phase-fields; weak Dirichlet boundary conditions

*Correspondence to: Department of Civil, Environmental, and Geo-Engineering, University of Minnesota, 500 Pillsbury Drive S.E., Minneapolis, MN 55455-0116, USA; Phone: +1 612 624-0063; Fax: +1 612 626-7750; E-mail: dominik@umn.edu

Contents

1	Introduction	3
2	Variational formulation and discretization	4
2.1	A simple model problem	4
2.2	The classical Nitsche approach in an embedded domain context	5
2.3	Phase-field approximation of volume and surface integrals	7
2.4	The diffuse Nitsche approach in a phase-field context	9
2.4.1	Diffuse boundary and diffuse volume	9
2.4.2	Diffuse boundary, but sharp volume	10
3	Element-wise stabilization	10
3.1	Coercivity and stabilization	11
3.1.1	Diffuse boundary and diffuse volume	11
3.1.2	Diffuse boundary, but sharp volume	12
3.2	Local evaluation of stabilization parameters	12
3.3	Elements with small support in the diffuse boundary region	14
4	Phase-field approximation and mixed meshes	15
4.1	Phase-field solutions of the Allen-Cahn equation	15
4.2	Phase-field discretization in space and time	17
4.3	Mixed meshes for phase-field and physics-based solutions	18
4.4	Adaptive quadrature based on recursive subdivision	18
5	Numerical tests, comparison with penalty-type methods, and surface-free analysis on imaging data	19
5.1	One-dimensional bar	20
5.2	Two-dimensional Laplace problem	24
5.3	Three-dimensional spherical thick shell	27
5.4	Relating phase-field length scale, voxel spacing and mesh size	33
5.5	Stress analysis of a patient-specific vertebra	34
6	Summary, conclusions and outlook	37

1. INTRODUCTION

Finite element methods based on diffuse boundaries [1, 2, 3, 4, 5, 6], also known as diffuse domain, phase-field, fat boundary or spread interface methods, provide a pathway for solving boundary value problems on very complex domains without the need for explicitly parameterizing boundary and interface surfaces. Various instantiations related to the phase-field concept have been published in the last few years, e.g., for advection-diffusion problems [7, 8], multi-phase flow [9, 10], the evolution of complex crack patterns [11, 12, 13, 14, 15], fluid infiltration and biomedical growth processes [16, 17, 18], and phase transition and segregation processes [19, 20, 21]. From a geometric point of view, their essential idea is to abandon the concept of sharply defined boundaries and instead approximate the domain implicitly by a phase-field function, which smoothly transitions from one inside the domain to zero in the exterior. The diffusiveness of the geometry approximation, i.e., the local slope of the phase-field at the boundary, can be controlled by a characteristic length-scale parameter. The phase-field approximation of the boundary and its gradient can then be employed to reformulate the boundary value problem on an extended regular domain. Boundary conditions originally formulated via surface terms are thus transferred into additional volumetric source terms, which completely eliminates the need for explicit boundary parametrizations. For Neumann-type boundary and interface conditions, this strategy leads to a straightforward phase-field approximation [22, 23]. For Dirichlet-type constraints, most of the attention has been focused on penalty-type approaches [4, 5, 24].

Embedded domain finite element methods, also known as fictitious domain or immersed boundary methods, represent another class of methods that are targeted at overcoming problems related to boundary-fitted meshing and parametrization of complex domains (see for example [25, 26, 27, 28, 29, 30, 31] and the references therein). In contrast to diffuse domain methods, they require an explicit sharp parameterization of embedded boundaries, e.g., in the form of B-rep surfaces [27, 32] or level-set functions [33, 34, 35]. Beyond their common motivation, embedded and diffuse domain methods share a number of fundamental methodological challenges. On the one hand, both require special attention towards the numerical integration of elements cut by boundaries. In this context, a series of papers have recently highlighted the importance of geometrically faithful quadrature in embedded domain methods (see for example [36, 37, 38, 39, 40, 41, 42] and the references therein).

On the other hand, both classes of methods require special techniques to enforce Dirichlet constraints at sharp and diffuse boundaries that arbitrarily cut through elements. For embedded domain methods, an important family of techniques that has attracted large attention in recent years revolves around the original idea of Nitsche who developed a variationally consistent method for weakly enforcing Dirichlet boundary conditions [43, 44, 45, 46]. In contrast to Lagrange multipliers [39, 47, 48], the Nitsche formulation is free of auxiliary fields, which simplifies the theory and reduces computational cost. The variational consistency of the symmetric Nitsche method allows the reinterpretation of the penalty parameter as a mesh dependent stabilization parameter that needs to be chosen sufficiently large as to maintain stability of the bilinear form. Suitable stabilization parameters can be estimated by an eigenvalue approach on a global level for the complete mesh [49] or on a local level for each intersected element [50, 51]. For embedded interface problems, an additional weighting of consistency terms can improve the accuracy [52, 53, 54].

In this paper, we combine the concept of diffuse domain methods with the idea of Nitsche's

method. We first derive a new diffuse variant of Nitsche's method that can effectively impose Dirichlet boundary conditions on phase-field boundaries. The variational formulation is then discretized with standard nodal elements, where we ensure the accurate integration of phase-field quantities by adapting the subdivision based quadrature technique of the finite cell method [55, 56]. To ensure coercivity of the discretized diffuse Nitsche formulation, we generalize the local eigenvalue technique, enabling the automatic estimation of appropriate element-wise stabilization parameters. We then demonstrate the numerical performance of the method with several examples in one, two and three dimensions. We compare the results with those obtained with a diffuse penalty-type method [24], which illustrates the improved accuracy and robustness of the diffuse Nitsche method.

From an engineering viewpoint, diffuse domain methods are particularly promising for the surface-free analysis of explicit geometric models based on imaging data. In this context, we combine the diffuse Nitsche method with voxel quadrature strategies to evaluate volume integrals directly on imaging data [23, 57]. We derive suitable relations between the three different length scales involved, that is, the length scale of the phase-field that controls the width of the diffuse boundary region, the voxel spacing that represents the resolution of the imaging data, and the mesh size that controls the accuracy of the approximation of the physics-based solution fields. Finally, we illustrate the versatility of this approach by a virtual compression test of a patient-specific bone structure that requires the imposition of Dirichlet boundary conditions on a complex CT-based geometry [23].

Our paper is organized as follows: In Section 2, we briefly review the standard sharp boundary form of Nitsche's method, discuss the derivation of phase-field approximations of volume and surface integrals and introduce the diffuse variant of Nitsche's method. In Section 3, we present the element-wise estimation of the stabilization parameter by a local eigenvalue problem. Section 4 discusses the set-up of an Allen-Cahn problem to generate suitable diffuse phase-field representations as well as the use of mixed meshes for the representation of the phase-field and physics-based solution fields. In Section 5, we present the results of the benchmark study that illustrates accuracy and convergence of the diffuse Nitsche method. In addition, we show the surface-free stress analysis of the CT-based vertebra, illustrating the strength of the new method for image-based simulation without explicit surface parametrization. Section 6 summarizes key aspects and draws conclusions.

2. VARIATIONAL FORMULATION AND DISCRETIZATION

In this section, we introduce the diffuse Nitsche method for a simple Poisson problem. We start from the variational formulation of the classical Nitsche method for weakly imposing Dirichlet boundary conditions on the sharply defined domain. We then discuss the approximation of volume and surface integrals by a diffuse phase-field representation defined on an embedding domain. We finally arrive at a diffuse formulation of Nitsche's method by inserting the phase-field approximations into the classical variational format.

2.1. A simple model problem

We consider the following Poisson problem

$$-\Delta u = f \quad \text{on } \Omega \tag{1}$$

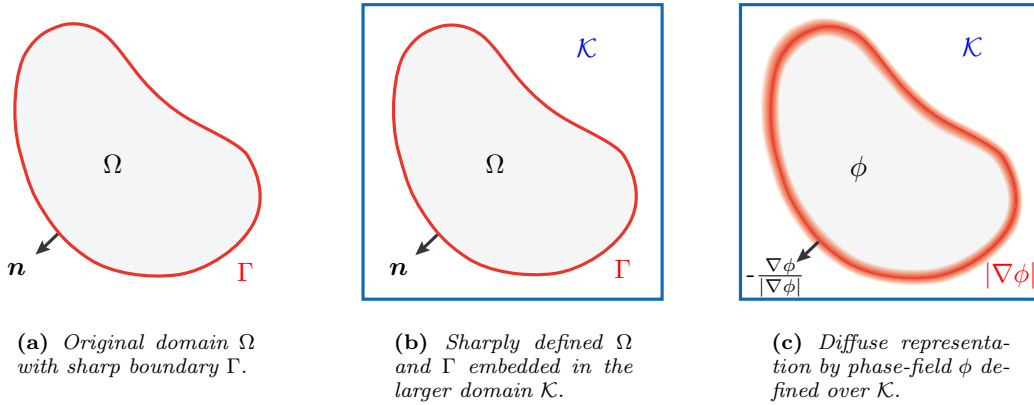


Figure 1: Volumes and surfaces in boundary-fitted, embedded domain and diffuse domain methods.

$$u = g \quad \text{on } \Gamma \quad (2)$$

where u is the unknown solution field, f is a known source term and g is a prescribed boundary function. We emphasize that the original problem definition (1) includes a well-defined domain Ω with a sharp Dirichlet boundary Γ of sufficient regularity as illustrated in Fig. 1a.

2.2. The classical Nitsche approach in an embedded domain context

There exist a variety of different methods to motivate the classical Nitsche method for weakly imposing Dirichlet boundary conditions, see [43, 46, 50] and the references therein. Here, we review its derivation through a flux formulation that originates in the interior penalty method [58, 59]. Following the unified framework in [59], we start the derivation of the variational form of Nitsche's method by rewriting the problem (1) as a first-order system

$$\boldsymbol{\sigma} = \nabla u, \quad -\nabla \cdot \boldsymbol{\sigma} = f \quad (3)$$

Multiplying the first and second equations by suitable test functions $\boldsymbol{\tau}$ and v and performing integration by parts, we find

$$\int_{\Omega} \boldsymbol{\sigma} \cdot \boldsymbol{\tau} \, d\Omega = - \int_{\Omega} u \nabla \cdot \boldsymbol{\tau} \, d\Omega + \int_{\Gamma} u \mathbf{n} \cdot \boldsymbol{\tau} \, d\Gamma \quad (4)$$

$$\int_{\Omega} \boldsymbol{\sigma} \cdot \nabla v \, d\Omega = \int_{\Omega} f v \, d\Omega + \int_{\Gamma} \boldsymbol{\sigma} \cdot \mathbf{n} v \, d\Gamma \quad (5)$$

where \mathbf{n} is the outward normal vector to Γ . We then discretize (4) and (5) in a Galerkin sense such that $\{u_h, \boldsymbol{\sigma}_h\} \in \mathcal{S}_h \subset L^2(\Omega)$ and $\{v_h, \boldsymbol{\tau}_h\} \in \mathcal{V}_h \subset H^1(\Omega)$, arriving at the *flux formulation* [59, 60]: For all v_h and $\boldsymbol{\tau}_h$, find u_h and $\boldsymbol{\sigma}_h$ such that

$$\int_{\Omega} \boldsymbol{\sigma}_h \cdot \boldsymbol{\tau}_h \, d\Omega = - \int_{\Omega} u_h \nabla \cdot \boldsymbol{\tau}_h \, d\Omega + \int_{\Gamma} \hat{u} \mathbf{n} \cdot \boldsymbol{\tau}_h \, d\Gamma \quad (6)$$

$$\int_{\Omega} \boldsymbol{\sigma}_h \cdot \nabla v_h \, d\Omega = \int_{\Omega} f v_h \, d\Omega + \int_{\Gamma} \hat{\boldsymbol{\sigma}} \cdot \mathbf{n} v_h \, d\Gamma \quad (7)$$

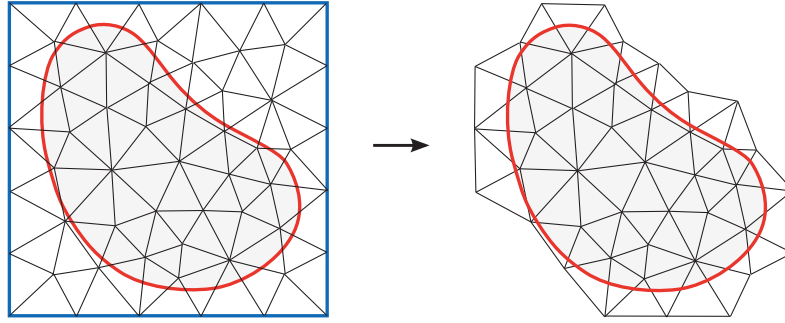


Figure 2: Discretization of the classical Nitsche method in an embedded domain context, referring to a sharp representation of the domain.

where the numerical fluxes $\hat{\boldsymbol{\sigma}}$ and \hat{u} are approximations to $\boldsymbol{\sigma} = \nabla u$ and to u on the Dirichlet boundary Γ . We employ definitions (6) and (7) on finite element meshes that have been generated by a discretization of an embedded domain \mathcal{K} (see Fig. 1b), where all elements located completely outside Ω are eliminated (see Fig. 2).

In the next step, we design expressions in terms of u_h for the numerical fluxes. To arrive at the classical Nitsche method, we choose

$$\hat{u} = g \quad (8)$$

$$\hat{\boldsymbol{\sigma}} = \nabla u_h - \beta (u_h - g) \mathbf{n} \quad (9)$$

Its final form is the primal formulation of (6) and (7), which can be obtained by relating $\boldsymbol{\sigma}$ and $\boldsymbol{\tau}$ to u and v . To this end, we first consider the integration by parts formula

$$-\int_{\Omega} u_h \nabla \cdot \boldsymbol{\tau}_h \, d\Omega = \int_{\Omega} \nabla u_h \cdot \boldsymbol{\tau}_h \, d\Omega - \int_{\Gamma} u_h \mathbf{n} \cdot \boldsymbol{\tau}_h \, d\Gamma \quad (10)$$

where we restrict $u_h \in \mathcal{V}_h \subset H^1(\Omega)$. Inserting (10) and the flux approximation (8) into (6) and identifying $\boldsymbol{\tau} = \nabla v$ yields the following expression

$$\int_{\Omega} \boldsymbol{\sigma}_h \cdot \nabla v_h \, d\Omega = \int_{\Omega} \nabla u_h \cdot \nabla v_h \, d\Omega + \int_{\Gamma} (g - u_h) \nabla v_h \cdot \mathbf{n} \, d\Gamma \quad (11)$$

Inserting the flux approximation (9) into (7) and relating the result to the left-hand side of (11) yields the following primal formulation: Find u_h such that we have

$$B(u_h, v_h) = \int_{\Omega} \nabla u_h \cdot \nabla v_h \, d\Omega - \int_{\Gamma} u_h \nabla v_h \cdot \mathbf{n} \, d\Gamma - \int_{\Gamma} \nabla u_h \cdot \mathbf{n} v_h \, d\Gamma + \beta \int_{\Gamma} u_h v_h \, d\Gamma \quad (12)$$

$$l(v_h) = \int_{\Omega} f v_h \, d\Omega - \int_{\Gamma} g \nabla v \cdot \mathbf{n} \, d\Gamma + \beta \int_{\Gamma} g v_h \, d\Gamma \quad (13)$$

where $B(u_h, v_h) = l(v_h)$. We observe that the classical Nitsche method (12) and (13) includes an additional parameter β that ensures that (12) satisfies the stability criterion (25) (see Section 3.1). We note that there exists a non-symmetric penalty-free variant of Nitsche's method that does not require stabilization [61, 62, 63].

2.3. Phase-field approximation of volume and surface integrals

From a geometric point of view, the diffuse Nitsche formulation is based on a diffuse approximation of the sharply defined domain Ω in terms of a phase-field function ϕ . The phase-field function ϕ can be perceived of as a regularized approximation of the Heaviside function H ,

$$H(\mathbf{x}) = \begin{cases} 1.0 & \forall \mathbf{x} \in \Omega \\ 0.0 & \text{otherwise} \end{cases} \quad (14)$$

which represents the sharp limit. It is defined on a larger embedding domain \mathcal{K} that completely contains the original problem domain $\Omega \subset \mathcal{K}$. The concept is illustrated in Fig. 1c for a two-dimensional domain, where the diffuse boundary region, i.e., the transition of the phase-field values from one to zero, are indicated by the blended area in red. The series of pictures shown Fig. 1a through 1c illustrates that the diffuse geometry idea can be perceived of as an extension of the classical embedded domain concept.

The reformulation of sharp integrals can then be achieved in the following way [3, 5, 24, 64]. We first consider a general volume integral on the original domain Ω . We can identify the following relations

$$\int_{\Omega} Q \, d\Omega = \int_{\mathcal{K}} Q H \, d\Omega \approx \int_{\mathcal{K}} Q \phi \, d\Omega \quad (15)$$

where Q is any well-behaved function to be integrated on Ω . We assume in (15) that the function Q can be extended beyond Ω such that the extension is constant in the normal direction off Γ [5, 24].

We then consider the diffuse representation of a surface integral on the sharp boundary surface Γ . We can identify the following relations

$$\int_{\Gamma} h \, d\Gamma = \int_{\mathcal{K}} h \delta_{\Gamma} \, d\Omega \approx \int_{\mathcal{K}} h |\nabla \phi| \, d\Omega \quad (16)$$

where the absolute value of the phase-field gradient approximates a Dirac δ distribution at the boundary Γ , that is

$$\delta_{\Gamma} \approx |\nabla \phi| \quad (17)$$

We again assume that h is any well-behaved function to be integrated on Γ that can be extended such that the extension is constant in the normal direction off Γ [5, 24].

Figure 3 plots a Heaviside function with a sharp boundary and several phase-field approximations along a one-dimensional section through the diffuse boundary region. We assume a characteristic length scale ε , with which we can control the width of the diffuse boundary region. We observe that the smaller the diffuse boundary width, the closer the phase-field approximates the Heaviside function. Figure 4 plots the absolute value of the gradient of the phase-field functions shown in Fig. 3. We observe that a decrease in the diffuse boundary width leads to a contraction of the gradient spike, which centers at the boundary location Γ .

To ensure consistent integration of the boundary function h , the absolute value of all phase-field gradient functions must reproduce the key property of a Dirac δ distribution, that is, their integrals across the interface width must be equal to 1. This fundamental requirement

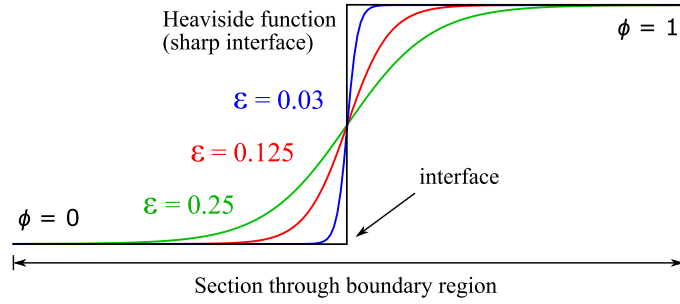


Figure 3: Phase-field functions ϕ of different characteristic length-scales ε as approximations of a sharp Heaviside function H .

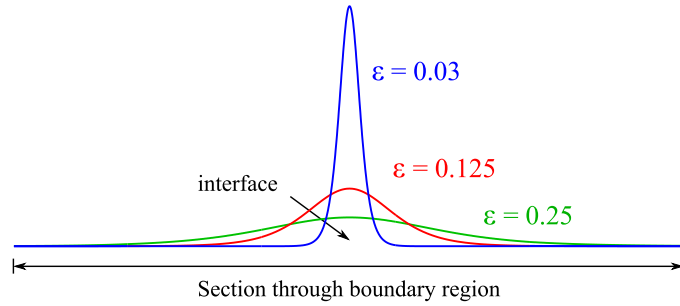


Figure 4: Absolute value of the gradient of the phase-field functions for different length-scales ε .

can be expressed concisely as

$$\int_{s_1}^{s_2} \delta_\Gamma ds = \int_{s_1}^{s_2} \left| \frac{d}{ds} \phi \right| ds = 1 \quad (18)$$

where s is an arbitrary straight line with starting and end points s_1 and s_2 that crosses the diffuse boundary region. One can easily verify that this property holds for any function that monotonically increases from zero to one (or monotonically decreases from one to zero).

Many surface integrals require a normal vector. The normal vector is directly obtained from the implicit phase-field representation as

$$\mathbf{n} \approx -\frac{\nabla \phi}{|\nabla \phi|} \quad (19)$$

where \mathbf{n} denotes the outward unit normal along the boundary of the physical domain Ω . This approximation that makes use of the steepest descent property of the gradient allows us to rewrite surface integrals that involve a normal in the following form

$$\int_\Gamma \mathbf{q} \cdot \mathbf{n} d\Gamma = \int_{\mathcal{K}} \mathbf{q} \cdot \mathbf{n} \delta_\Gamma d\Omega \approx -\int_{\mathcal{K}} \mathbf{q} \cdot \nabla \phi d\Omega \quad (20)$$

where \mathbf{q} denotes an arbitrary flux quantity.

In summary, we note that relations (15) through (20) are valid for any phase-field function ϕ that satisfies the following four key requirements:

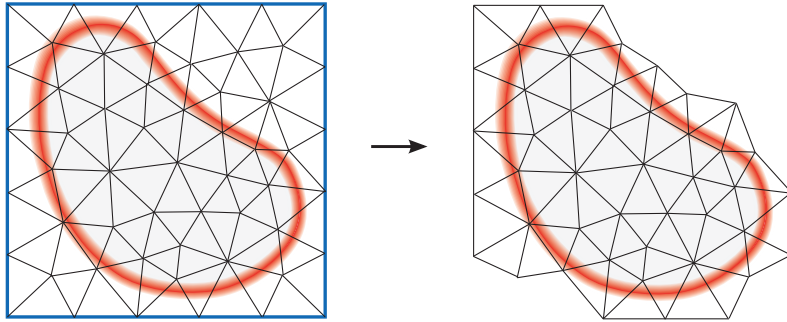


Figure 5: Discretization of the diffuse Nitsche method, based on a diffuse representation of the domain.

1. The phase-field is a monotonically decreasing function from one in the original problem domain Ω to zero outside (see Fig. 3).
2. With decreasing length scale of the diffuse boundary region, the phase-field converges to the Heaviside function H (14).
3. Given sufficient regularity of Γ , the negative normalized gradient of the phase-field converges to the boundary normal.
4. The center line of the diffuse boundary corresponds to the sharp boundary.

2.4. The diffuse Nitsche approach in a phase-field context

Given a suitable phase-field representation ϕ , we are now in a position to derive a geometrically diffuse formulation of Nitsche's method. To this end, we consider again the discretized classical formulation of Nitsche's method (12) and (13) that is defined over sharply defined volume and boundary surface representations Ω and Γ . We assume that all properties of the discrete space \mathcal{V}_h extend through the diffuse boundary region into the embedding domain \mathcal{K} , so that we obtain discrete functions $\{u_h, v_h\} \in \mathcal{V}_h \subset H^1(\mathcal{K})$.

2.4.1. Diffuse boundary and diffuse volume We can then derive a first diffuse Nitsche variant along the lines of classical diffuse domain methods [3, 5, 24], where we consider phase-field approximations for both volume and surface integrals in (12) and (13). To this end, we employ the identities (15) and (16) to replace integrals over the physical domain Ω and its sharp boundary Γ by integrals over the embedding domain \mathcal{K} . The result is the following geometrically diffuse formulation: Find u_h such that $B(u_h, v_h) = l(v_h)$ for all v_h , where we have

$$B(u_h, v_h) = \int_{\mathcal{K}} \nabla u_h \cdot \nabla v_h \phi \, d\Omega + \int_{\mathcal{K}} u_h \nabla v_h \cdot \nabla \phi \, d\Omega + \int_{\mathcal{K}} \nabla u_h \cdot \nabla \phi v_h \, d\Omega + \beta \int_{\mathcal{K}} u_h v_h |\nabla \phi| \, d\Omega \quad (21)$$

$$l(v_h) = \int_{\mathcal{K}} f v_h \phi \, d\Omega + \int_{\mathcal{K}} g \nabla v_h \cdot \nabla \phi \, d\Omega + \beta \int_{\mathcal{K}} g v_h |\nabla \phi| \, d\Omega \quad (22)$$

The diffuse formulation involves only volumetric integrals, since all surface terms have been transferred into volumetric source terms.

We evaluate the terms in (21) and (22) on finite element meshes that have been generated by a discretization of the embedding domain \mathcal{K} . All elements located outside the diffuse volume and “sufficiently away” from the diffuse boundary region can be eliminated. Figure 5 illustrates that due to the extension of the diffuse boundary region beyond the sharp domain, the diffuse domain mesh needs to retain more elements at the boundary than the embedded domain mesh in Fig. 2 that refers to a sharp representation of the domain. In the next section, we will discuss practical rules on how to determine whether an element can be eliminated.

2.4.2. Diffuse boundary, but sharp volume A promising application of diffuse domain methods that we will consider in Section 5 is the analysis of complex geometries based on imaging data. On the one hand, imaging data can be leveraged to design quadrature techniques that are able to evaluate sharp volume integrals down to pixel resolution. An example is the voxel finite cell method that uses pre-integration of voxel sub-domains to efficiently evaluate stiffness forms in real time [23, 57, 65]. On the other hand, the evaluation of integrals over sharp boundary surfaces requires image segmentation and surface reconstruction. Eliminating the need for explicit surface parameterizations, the diffuse formulation offers an opportunity to circumvent the associated time-consuming image processing and geometry operations.

With these considerations in mind, we derive a second diffuse variant of Nitsche’s method, where we consider only phase-field approximations for the boundary surface integrals, but leave the volume integrals in sharp format. Starting from the geometrically diffuse formulation (21) and (22) and corresponding finite element discretizations illustrated in Fig. 5, we convert all diffuse volume terms back to their sharp representation by replacing the phase-field function ϕ by its sharp boundary limit H in the sense of (15). The resulting sharp domain, but diffuse boundary formulation follows as: Find u_h such that $B(u_h, v_h) = l(v_h)$ for all v_h , where

$$B(u_h, v_h) = \int_{\mathcal{K}} \nabla u_h \cdot \nabla v_h H \, d\Omega + \int_{\mathcal{K}} u_h \nabla v_h \cdot \nabla \phi \, d\Omega + \int_{\mathcal{K}} \nabla u_h \cdot \nabla \phi v_h \, d\Omega + \beta \int_{\mathcal{K}} u_h v_h |\nabla \phi| \, d\Omega \quad (23)$$

$$l(v_h) = \int_{\mathcal{K}} f v_h H \, d\Omega + \int_{\mathcal{K}} g \nabla v_h \cdot \nabla \phi \, d\Omega + \beta \int_{\mathcal{K}} g v_h |\nabla \phi| \, d\Omega \quad (24)$$

where H denotes the Heaviside function (14). In the following, we focus primarily on the diffuse variant (23) and (24) due to its significance for image based analysis.

3. ELEMENT-WISE STABILIZATION

In this section, we derive conditions for coercivity of the discrete diffuse Nitsche forms, arriving at local estimates for the stabilization parameter for both diffuse variants discussed above. A particular focus lies on the estimation of the stabilization parameter in the diffuse boundary, but sharp volume case, where elements might have a small support in the diffuse boundary region, but no support in the sharp volumetric domain.

3.1. Coercivity and stabilization

We start by examining coercivity of the discrete bilinear forms (21) and (23). We recall that for coercivity to hold, any discrete bilinear form needs to satisfy the following condition [66]:

$$B(v_h, v_h) \geq 0 \quad (25)$$

where we use $v_h \in \mathcal{V}_h \subset H^1(\mathcal{K})$ in place of u_h . We present our analysis for the Poisson model problem (1) and (2) introduced in Section 2.1, but note that it is straightforward to extend our presentation to boundary value problems with other differential operators. Our approach is closely linked to the standard analysis approach and eigenvalue based estimation techniques that have been successfully established for the classical Nitsche method, see for example [46, 49, 50, 51, 54, 67]. For ease of notation, we will make use of the definition of the L^2 norm defined for an arbitrary function w over the embedding domain \mathcal{K} as

$$\|w\| = \left(\int_{\mathcal{K}} w^2 \, d\Omega \right)^{1/2} \quad (26)$$

3.1.1. Diffuse boundary and diffuse volume When we use the discrete form (21), i.e., both the volumetric domain and its boundary are represented in terms of a diffuse phase-field, the discrete bilinear form for the Poisson model problem can be written as follows

$$B(v_h, v_h) = \int_{\mathcal{K}} \nabla v_h \cdot \nabla v_h \phi \, d\Omega + 2 \int_{\mathcal{K}} v_h (\nabla v_h \cdot \nabla \phi) \, d\Omega + \beta \int_{\mathcal{K}} (v_h)^2 |\nabla \phi| \, d\Omega \quad (27)$$

It can be simplified with (26) as

$$B(v_h, v_h) = \|\nabla v_h \sqrt{\phi}\|^2 + 2 \int_{\mathcal{K}} v_h (\nabla v_h \cdot \nabla \phi) \, d\Omega + \beta \|v_h \sqrt{|\nabla \phi|}\|^2 \quad (28)$$

where we make use of the positivity of the phase-field function ϕ . We now find an upper bound of the function in the second term as

$$|v_h (\nabla v_h \cdot \nabla \phi)| \leq |v_h| |\nabla v_h| |\nabla \phi| = |v_h| \sqrt{|\nabla \phi|} |\nabla v_h| \sqrt{|\nabla \phi|} \quad (29)$$

Using Young's inequality with $\kappa > 0$, the integral of the absolute value of the original function can then be bounded as follows

$$2 \int_{\mathcal{K}} |v_h (\nabla v_h \cdot \nabla \phi)| \, d\Omega \leq \kappa^{-1} \int_{\mathcal{K}} (|v_h| \sqrt{|\nabla \phi|})^2 \, d\Omega + \kappa \int_{\mathcal{K}} (|\nabla v_h| \sqrt{|\nabla \phi|})^2 \, d\Omega \quad (30)$$

This represents an upper bound on the second term in (28). However, this term can potentially be negative, we require a lower bound on its negative value, which we can simply obtain by multiplying (28) with a minus sign. We hence obtain the following lower bound

$$-2 \int_{\mathcal{K}} |v_h (\nabla v_h \cdot \nabla \phi)| \, d\Omega \geq -\kappa^{-1} \|v_h \sqrt{|\nabla \phi|}\|^2 - \kappa \|\nabla v_h \sqrt{|\nabla \phi|}\|^2 \quad (31)$$

Using (31) in (28), we can bound $B(v_h, v_h)$ from below as follows

$$B(v_h, v_h) \geq \|\nabla v_h \sqrt{\phi}\|^2 - \kappa \|\nabla v_h \sqrt{|\nabla \phi|}\|^2 - \kappa^{-1} \|v_h \sqrt{|\nabla \phi|}\|^2 + \beta \|v_h \sqrt{|\nabla \phi|}\|^2 \quad (32)$$

Following [49, 51, 68], we design a generalized inverse estimate for the diffuse case. It postulates that there exists a configuration-dependent constant $C_1 > 0$ such that

$$\|\nabla v_h \sqrt{|\nabla\phi|}\|^2 \leq C_1 \|\nabla v_h \sqrt{\phi}\|^2 \quad (33)$$

We note that we use subscript $i = \{1, 2\}$ in order to distinguish between the constants C_i computed from the two variants of Nitsche's method (33) and (39). Replacing the second term in (32) by the inequality (33) and collecting terms, we find

$$B(v_h, v_h) \geq (1 - \kappa C_1) \|\nabla v_h \sqrt{\phi}\|^2 + (\beta - \kappa^{-1}) \|v_h \sqrt{|\nabla\phi|}\|^2 \quad (34)$$

Since Young's inequality allows us to choose an arbitrary $\kappa > 0$, we assume $\kappa = 1/C_1$ such that the first term in (34) cancels. It is then straightforward to see that for (25) to hold, the stabilization parameter β needs to satisfy the following condition:

$$\beta \geq C_1 \quad (35)$$

3.1.2. Diffuse boundary, but sharp volume When we use the discrete form (23), only integrals associated with the boundary employ the diffuse phase-field representation, but all terms associated with volume integrals use a sharp representation in terms of a Heaviside function H . The discrete bilinear form for the Poisson model problem can then be written as follows

$$B(v_h, v_h) = \int_{\mathcal{K}} \nabla v_h \cdot \nabla v_h H \, d\Omega + 2 \int_{\mathcal{K}} v_h (\nabla v_h \cdot \nabla\phi) \, d\Omega + \beta \int_{\mathcal{K}} (v_h)^2 |\nabla\phi| \, d\Omega \quad (36)$$

which we again simplify with (26) as

$$B(v_h, v_h) = \|\nabla v_h \sqrt{H}\|^2 + 2 \int_{\mathcal{K}} v_h (\nabla v_h \cdot \nabla\phi) \, d\Omega + \beta \|v_h \sqrt{|\nabla\phi|}\|^2 \quad (37)$$

Estimating the second term in (37) from below as in (32), we can transform (37) into

$$B(v_h, v_h) \geq \|\nabla v_h \sqrt{H}\|^2 - \kappa \|\nabla v_h \sqrt{|\nabla\phi|}\|^2 - \kappa^{-1} \|v_h \sqrt{|\nabla\phi|}\|^2 + \beta \|v_h \sqrt{|\nabla\phi|}\|^2 \quad (38)$$

Following (33), we postulate a configuration-dependent constant $C_2 > 0$ such that

$$\|\nabla v_h \sqrt{|\nabla\phi|}\|^2 \leq C_2 \|\nabla v_h \sqrt{H}\|^2 \quad (39)$$

We now use C_2 in (38) and consolidate terms as in (34), assuming that $\kappa = 1/C_2$. We then find that coercivity is satisfied, if $\beta \geq C_2$.

3.2. Local evaluation of stabilization parameters

The expressions for β guarantee stability of the diffuse Nitsche method, but involve constants C_1 and C_2 that need to be evaluated. We follow the approach discussed by GRIEBEL and SCHWEITZER [49] and elaborated by DOLBOW, HARARI and collaborators [46, 50, 51, 52, 53, 54, 69]. It is based on the concept of transferring the inequalities (33) and (39) into a generalized eigenvalue problem, from which a set of eigenvalues can be computed. The constants are bounded from below by the maximum eigenvalue.

We briefly illustrate this strategy for the Poisson model problem. We start by rewriting the discrete function v_h and its gradient ∇v_h in matrix format:

$$v_h = \sum_i^n N_i c_i = [N_1 \ N_2 \ \dots \ N_n]_{1 \times n} \mathbf{c} = \mathbf{N} \mathbf{c} \quad (40)$$

$$\nabla v_h = \sum_i^n \nabla N_i c_i = [\nabla N_1 \ \nabla N_2 \ \dots \ \nabla N_n]_{d \times n} \mathbf{c} = \mathbf{N}_{,\mathbf{x}} \mathbf{c} \quad (41)$$

where N_i denotes the i^{th} basis function, \mathbf{c} is a vector of coefficients, and d is the spatial dimension. Using definition (26), we rewrite the inequality (33) in explicit integral format,

$$\int_{\mathcal{K}} \nabla v_h \cdot \nabla v_h |\nabla \phi| \, d\Omega \leq C_1 \int_{\mathcal{K}} \nabla v_h \cdot \nabla v_h \phi \, d\Omega \quad (42)$$

and find the corresponding matrix format by inserting (40) and (41),

$$\mathbf{c}^T \int_{\mathcal{K}} \mathbf{N}_{,\mathbf{x}}^T \mathbf{N}_{,\mathbf{x}} |\nabla \phi| \, d\Omega \mathbf{c} \leq C_1 \mathbf{c}^T \int_{\mathcal{K}} \mathbf{N}_{,\mathbf{x}}^T \mathbf{N}_{,\mathbf{x}} \phi \, d\Omega \mathbf{c} \quad (43)$$

It is easy to see that for the diffuse boundary, but sharp volume case the constant C_2 in (39) can be computed in the same fashion, if we replace the diffuse phase-field function ϕ by the sharp Heaviside function H in the right-hand side of (42), leading to the following inequality

$$\mathbf{c}^T \int_{\mathcal{K}} \mathbf{N}_{,\mathbf{x}}^T \mathbf{N}_{,\mathbf{x}} |\nabla \phi| \, d\Omega \mathbf{c} \leq C_2 \mathbf{c}^T \int_{\mathcal{K}} \mathbf{N}_{,\mathbf{x}}^T \mathbf{N}_{,\mathbf{x}} H \, d\Omega \mathbf{c} \quad (44)$$

We can then define an associated generalized eigenvalue problem of the following form

$$\mathbf{A} \mathbf{c} = \lambda \mathbf{B} \mathbf{c} \quad (45)$$

where matrices \mathbf{A} and \mathbf{B} are computed by the integral expressions on the left-hand and right-hand sides of (43) and (44), respectively. When C_1 , or C_2 , corresponds to the maximum eigenvalue λ_{\max} defined by the eigenvalue problem (45), the inequality (43), or (44), holds for any vector of coefficients \mathbf{c} . We briefly sketch the corresponding proof in the remark below.

As the bilinear form is assembled from local components, the global coercivity argument (25) can be written as

$$B(v_h, v_h) = \sum_{n_{\text{el}}} B_{\text{el}}(v_{h,\text{el}}, v_{h,\text{el}}) \geq 0 \quad (46)$$

where n_{el} denotes the total number of elements and $v_{h,\text{el}}$ is the restriction of v_h on each element domain. It is now straightforward to see that if we guarantee that coercivity is satisfied locally on each element, $B_{\text{el}}(v_{h,\text{el}}, v_{h,\text{el}}) \geq 0$, coercivity holds globally via (46). The localization argument (46) allows us to break down the global statements (40) through (45) to corresponding element-wise statements. The resulting element-wise eigenvalue problems (45) define element-wise stabilization parameters, are small and inexpensive to compute, and can be evaluated in parallel in the context of element-centered formation and assembly algorithms.

Remark 1: The following arguments show that the inequality (42) is satisfied, if we use $C_1 = \lambda_{\max}$. We can assume that any function v_h can be represented as a combination of linearly independent eigenvectors of (45), $\hat{\mathbf{c}}_i$, times corresponding basis functions in row vector format, \mathbf{N} , and coefficients, a_i , in the following form

$$v_h = \sum_i \mathbf{N} \hat{\mathbf{c}}_i a_i \quad (47)$$

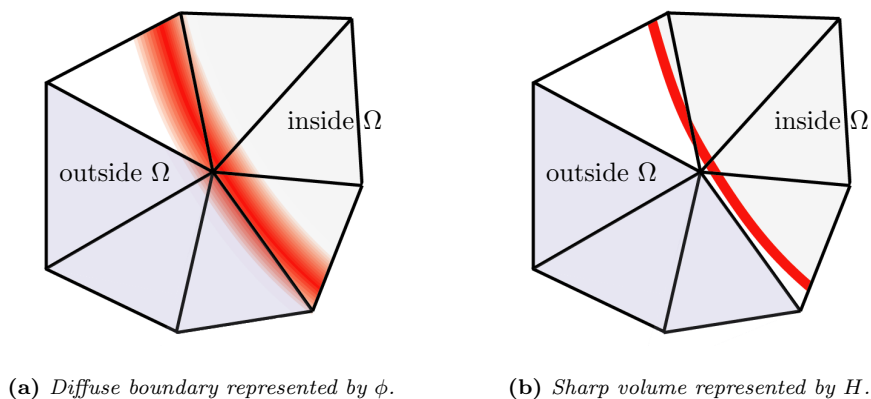


Figure 6: Embedding element patch: Since the diffuse boundary region extends beyond the original domain, gray-shaded elements have support in the diffuse boundary region, but not in the sharp volume.

Inserting the decomposition (47) into the left hand side of inequality (43), we can write

$$\sum_i (a_i \hat{\mathbf{c}}_i)^T \mathbf{A} \sum_j (a_j \hat{\mathbf{c}}_j) = \sum_i (a_i \hat{\mathbf{c}}_i)^T \sum_j (a_j \lambda_j \mathbf{B} \hat{\mathbf{c}}_j) = \sum_i \sum_j \left(a_i a_j \lambda_j \hat{\mathbf{c}}_i^T \mathbf{B} \hat{\mathbf{c}}_j \right) \quad (48)$$

where we use matrices \mathbf{A} and \mathbf{B} as defined in (42) and (43). It is easy to see that for (48) to hold, all quantities in the last bracket need to be positive. To this end, we recall the following set of arguments: For the differential operators considered here, both \mathbf{A} and \mathbf{B} are symmetric and positive definite. In addition, we assume that we can exclude repeated eigenvalues. It can therefore be shown that $\hat{\mathbf{c}}_i^T \mathbf{B} \hat{\mathbf{c}}_j = 0$ for $i \neq j$, $\hat{\mathbf{c}}_i^T \mathbf{B} \hat{\mathbf{c}}_i > 0$ and all eigenvalues λ_i are positive [70]. Using these arguments, we can establish the following inequality from (48):

$$\sum_i (a_i \hat{\mathbf{c}}_i)^T \mathbf{A} \sum_j (a_j \hat{\mathbf{c}}_j) = \sum_i \left(a_i^2 \lambda_i \hat{\mathbf{c}}_i^T \mathbf{B} \hat{\mathbf{c}}_i \right) \leq \lambda_{\max} \sum_i \left(a_i^2 \hat{\mathbf{c}}_i^T \mathbf{B} \hat{\mathbf{c}}_i \right) \quad (49)$$

which corresponds to the inequality (43) and where we identify $C_1 = \lambda_{\max}$. The same arguments hold for the determination of C_2 based on inequality (39).

3.3. Elements with small support in the diffuse boundary region

The eigenvalue problem established in equations (40) through (45) and the localization argument (46) provide a framework for computing a suitable stabilization parameter β in each element that has support in the diffuse boundary region. If we consider the case of diffuse approximations of both the boundary and the volume, this strategy can be directly applied without restriction. There exist configurations, however, where the eigenvalue problem (45) is ill-posed, if we consider a diffuse approximation for the boundary surface only, but maintain a sharp definition for the volume. These configurations correspond to elements with small cuts, such that the diffuse boundary region does not run through the center of the element, but covers only a small portion of the element domain close to the element periphery.

We illustrate the issue with a patch of elements of an embedding domain mesh shown in Fig. 6. We observe that the three elements in gray on the lower-left side have support in the

diffuse boundary region, and hence need to be retained in the embedding mesh. But they do not have support in the original sharp domain, represented by the non-zero part of the Heaviside function H as defined in (14). When evaluating the left-hand side integral in (44) associated with the diffuse boundary region, we obtain a well-defined matrix \mathbf{A} as the diffuse boundary region has a non-zero support in each element. The right-hand side integral in (44) associated with the sharp Heaviside function H , however, leads to a singular matrix \mathbf{B} , since rows and columns associated with those basis functions that are only defined over the gray-shaded elements are zero due to the missing support of the non-zero part of H .

There are different strategies to mitigate this problem. A naive solution is to eliminate all elements with support in the diffuse boundary region, but without support in the sharp volume. Another idea is to maintain the elements, but eliminate all basis functions that have no support in the sharp volume. We found, however, that both variants negatively affect the method's accuracy. In the scope of the present work, we adopt the idea of stabilizing the "fictitious" element domain outside the original domain by adding a small additional "stiffness", which has been successfully applied, e.g., in early variants of the high-order finite cell method [55, 71]. We therefore consider a modified Heaviside function defined as

$$H(\mathbf{x}) = \begin{cases} 1.0 & \forall \mathbf{x} \in \Omega \\ \alpha & \text{otherwise} \end{cases} \quad (50)$$

where $\alpha \ll 1$ is a small stabilization parameter that guarantees that matrix \mathbf{A} in (44) remains well-defined. In this work, we use $\alpha = 10^{-8}$ in all examples. The stabilization idea based on (50) is simple to implement, effective and we have not observed any impact on the accuracy of the diffuse domain method for the accuracy levels considered in this work.

4. PHASE-FIELD APPROXIMATION AND MIXED MESHES

The diffuse Nitsche method relies on the availability of a suitable diffuse geometry model. In the next step, we discuss the construction of phase-field approximations of sharp domains that evolve from the short-term dynamic solution of an initial boundary value problem based on the Allen-Cahn equation. We also outline its discretization in time and space, using a semi-implicit time integration scheme and finite element meshes that are adaptively refined in the diffuse boundary region. We apply mixed meshes, such that the phase-field can be represented by a mesh that is much finer than the mesh for the physics-based solution. In this context, we also discuss an adaptive quadrature scheme that enable the accurate resolution of phase-field quantities in the coarser elements of the physics-based solution.

4.1. Phase-field solutions of the Allen-Cahn equation

We consider the initial boundary value problem based on the Allen-Cahn equation

$$\frac{\partial \phi}{\partial t} = \varepsilon^2 \nabla^2 \phi - \frac{\partial F(\phi)}{\partial \phi} \quad \text{on } \mathcal{K} \times (0, T) \quad (51)$$

$$\nabla \phi \cdot \mathbf{n} = 0 \quad \text{at } \partial \mathcal{K} \quad (52)$$

$$\phi(\mathbf{x}) = H \quad \text{at } t = 0 \quad (53)$$

where ε denotes again a characteristic length scale, with which we can control the width of the diffuse interface region.

Following FENTON et al. [64], we choose the potential function $F(\phi)$ as a double-well potential

$$F(\phi) = -\frac{(2\phi - 1)^2}{4} + \frac{(2\phi - 1)^4}{8} = 2\phi^2(\phi - 1)^2 - \frac{1}{8} \quad (54)$$

with minima at $\phi = 0$ and $\phi = 1$. As a result, the phase-field solution $\phi(\mathbf{x}, t)$ separates into two regions at values zero and one, while the diffusion operator tends to smooth out the spatial discontinuity of ϕ at the interface between these two regions [64, 72] (see also Fig. 3). The balance between the double-well potential and the diffusion operator leads to a diffuse boundary region, whose width is controlled by the length-scale parameter ε . In line with the double-well potential, we choose the Heaviside function (14) as the initial condition, which characterizes the sharply defined domain with an explicit boundary surface. The Heaviside function can be directly derived from implicit representations of the geometry, e.g., an analytical expression, or from explicit imaging data (see Section 5). With (54), the one-dimensional steady-state phase-field solution of (51) in an infinite half space with boundary $x = a$ is given by

$$\phi(x) = \frac{1}{2} \left(1 - \tanh \left(\frac{x - a}{\varepsilon} \right) \right) \quad (55)$$

The diffuse functions plotted in Fig. 3 correspond to (55) with different values of ε . Functions of the form (55) satisfy all requirements stated in Section 2.3.

The dynamic behavior of the Allen-Cahn equation has been studied in [72]. Before reaching its steady-state, the solution passes through different evolution phases, each characterized by a certain time scale. In the present scope, we are only interested in the short-term dynamics. At first, given a random initial condition, the forcing associated with $\partial_\phi F(\phi)$ dominates the solution behavior, driving the initial data at each point to the closest minimum of the potential (54). As the phase-field values locally approach the two minima, the effect of $\partial_\phi F(\phi)$ decreases. At an interface, the forcing that wants to form a jump in ϕ starts to compete with the effect of the diffusion term. This leads to the formation of a diffuse region instead of a sharp jump. The result is a smooth phase-field function that we adopt as our diffuse geometry model.

The short-term phase-field solutions, also called metastable patterns, are extremely resilient and stable over a long period of time [72]. They therefore constitute a quasi-steady-state solution that can be computed reliably and efficiently. On the long-term time scale, however, diffuse boundaries will eventually start to move and dissipate. While metastable patterns have fully formed at a time scale of order ε^{-1} , the time scale associated with the start of the annihilation and coalescence is at least of order $e^{l/\varepsilon}$, where l corresponds to the smallest distance separating two boundaries [73].

Remark 2: The one-dimensional solution (55) of the phase-field function motivates a generalization for arbitrary diffuse geometries in multiple dimensions in the following form

$$\phi(\mathbf{x}) = \frac{1}{2} \left(1 - \tanh \left(\frac{r(\mathbf{x})}{\varepsilon} \right) \right) \quad (56)$$

where $r(\mathbf{x})$ denotes the signed distance function from any point \mathbf{x} to the closest boundary Γ . The function r is assumed positive in the sharply defined original domain Ω and negative

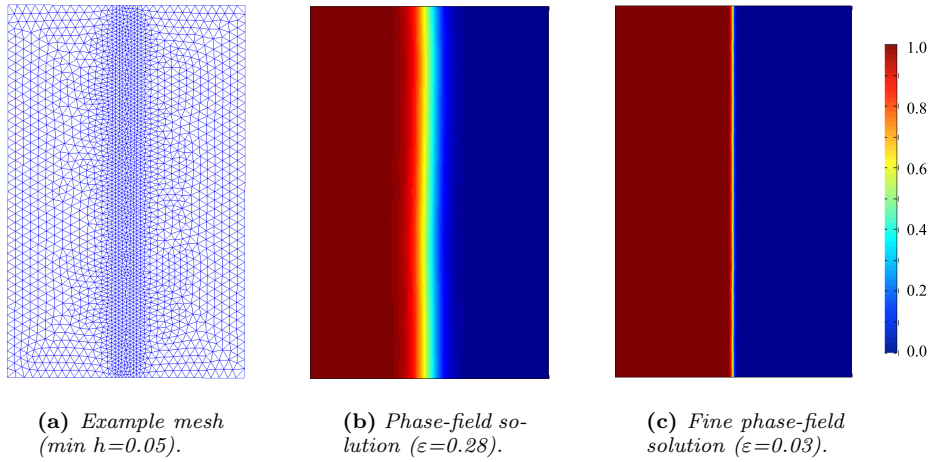


Figure 7: Diffuse geometry example with straight boundary. Phase-field solutions are computed for different length-scale parameters ε on adaptive meshes with minimum local mesh size $h = \varepsilon$.

outside, where the sharp boundary is given by the level set $\phi = 1/2$ [3, 5]. Expression (56) is attractive if a signed distance function is readily available, for example in the case of simple analytical shapes such as circles or spheres.

4.2. Phase-field discretization in space and time

We discretize the variational weak form of (51) with standard nodal finite elements in space and in time with a second-order semi-implicit scheme based on a backward differentiation formula (BDF) and Adams-Bashforth methods [74]. The time-discretized variational form reads

$$\frac{1}{2\Delta t} \int (3\phi^{n+1} - 4\phi^n + \phi^{n-1}) \psi \, d\Omega + \varepsilon^2 \int \nabla \phi^{n+1} \cdot \nabla \psi \, d\Omega + \int (2F'(\phi^n) - F'(\phi^{n-1})) \psi \, d\Omega = 0 \quad (57)$$

where Δt is the time step size, n denotes the current time step, and ψ is a test function. The time integration scheme (57) is simple to implement, second-order accurate and energy-stable for reasonably small time steps (see [74] for the stability criterion).

In practice, we integrate the discretized variational form (57) until a reasonably smooth diffuse boundary has been achieved, following the short-term dynamic behavior of the Allen-Cahn equation discussed above. We assume that we have achieved the metastable state when the 2-norm of the difference between the phase-field solutions at the previous and current time steps falls below a specified fraction of the initial difference between the first two time steps.

The width of the diffuse boundary is approximately 4ε [64] and needs to be resolved by a sufficiently fine mesh size in its vicinity. Therefore, the local mesh size h has to be proportional to the length scale ε of the diffuse interface. Figure 7 illustrates the method for a simple geometry with a straight diffuse boundary. Adaptivity is driven by the criterion to achieve a local mesh size of $h = \varepsilon$ in the vicinity of the diffuse boundary region.

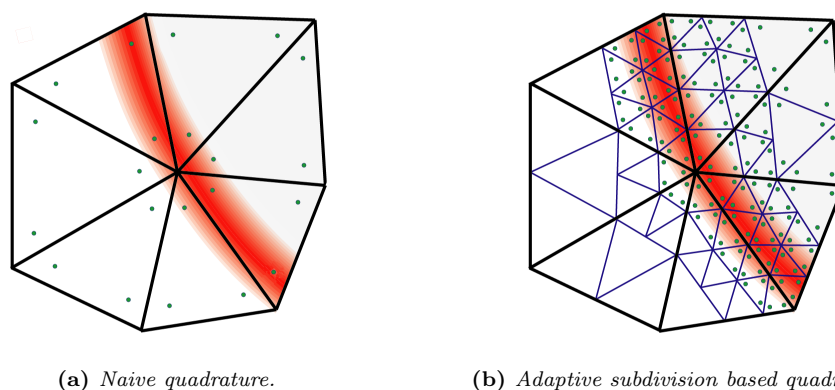


Figure 8: Volumetric integrals that involve phase-field quantities require special quadrature techniques that sufficiently resolve phase-field quantities in the diffuse boundary region. The dots represent quadrature points taken into account during numerical integration.

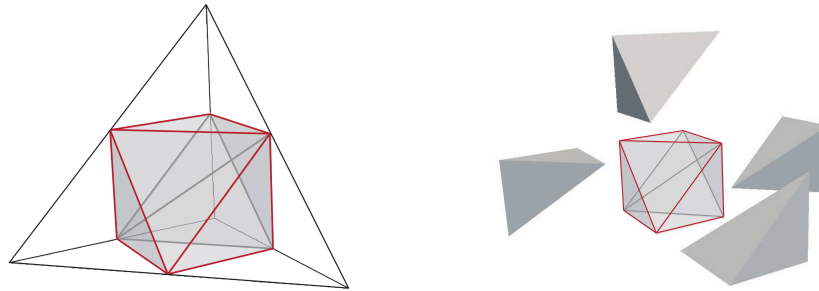
4.3. Mixed meshes for phase-field and physics-based solutions

For practical levels of accuracy in the physics-based solution, the characteristic length-scale ε of the phase-field must be significantly smaller than the mesh size for the physics-based solution fields. If the phase-field is obtained as the solution of an initial boundary value problem, small length scales require a very fine mesh along the diffuse boundary region to resolve the phase-field gradient. The physics-based solution fields, however, typically do not require the same fine mesh grading at the boundary, so that using the same meshes leads to an overkill in degrees of freedom on this end. This inefficiency can be eliminated by the use of different meshes for approximating the phase-field and physics-based solutions, which enables individual grading of the mesh size in the diffuse boundary region.

In general, the use of mixed meshes significantly reduces the number of degrees of freedom for the discretization of the diffuse Nitsche method. On the one hand, this is particularly important, as the physics-based discrete systems of diffuse domain methods are typically not well-conditioned due to the presence of small cuts, therefore mostly relying on direct solvers. In addition, they often grow faster in size due to multiple degrees of freedom per basis functions. On the other hand, the discretization of the Allen-Cahn problem (51) through (53) is much simpler to solve, as it leads to discrete systems that can be efficiently solved by standard parallelized pre-conditioning and iterative solvers. In addition, the phase-field is always scalar with a single degree of freedom per basis function.

4.4. Adaptive quadrature based on recursive subdivision

If the length scale of the phase-field function is smaller than the mesh size h of the physics-based solution fields, standard quadrature rules are insufficient in elements cut by the diffuse boundary region. This is illustrated in Fig. 8a for a patch of triangular elements, where the ratio ε/h is approx. $1/10$. We observe that with standard 3-point quadrature in each element, an accurate integration of phase-field quantities in the variational forms (21) through (24) is not possible, as only a few quadrature points are located in the diffuse boundary region.

(a) *Separate the four corner sub-cells first.*(b) *Split octahedron into four sub-cells.***Figure 9:** *Building block of the recursive subdivision approach: a tetrahedron is split into 8 sub-cells.*

In this work, we resolve this issue by adjusting the adaptive subdivision based quadrature scheme of the finite cell method [56, 55], which is based on the recursive split of intersected elements in quadrature sub-cells. For the phase-field case, the scheme is illustrated in Fig. 8b for the triangular patch. Its basic building block is the split of all intersected triangles into four smaller triangles. This split is then repeated recursively for each intersected sub-cell until a predefined minimum sub-cell size is reached. In each sub-cell, we individually apply standard quadrature rules, where the weights of the quadrature points are scaled with the volume of the sub-cell. Figure 8b shows that this strategy leads to an aggregation of quadrature points in the diffuse boundary region. Sub-cells that are completely located in element areas where the phase-field is zero can be omitted in the integration process. We emphasize that subdivision only affects the definition of quadrature points, but leaves basis functions untouched, which are still defined on the original elements. To help clearly distinguish between the two entities, we will plot elements with basis functions in black and quadrature sub-cells in blue.

The adaptive subdivision based quadrature scheme can be easily generalized to different element types [55, 75, 76]. For tetrahedral elements applied in this work, the basic building block is the split of an intersected tetrahedron into eight tetrahedral sub-cells as shown in Fig. 9. From an algorithmic viewpoint, we implement recursive subdivision in a “bottom-up” fashion [75]. We first refine the complete tetrahedral element by generating all possible leaves at the maximum tree depth. We then start to build up the sub-cell tree by combining sets of uncut sub-cells into one sub-cell of higher level. This pruning procedure is repeated recursively until we reach the original finite element, using the phase-field as an indicator function to determine whether quadrature points of a sub-cell are located inside the physical domain, in the diffuse boundary region or completely outside the diffuse domain.

5. NUMERICAL TESTS, COMPARISON WITH PENALTY-TYPE METHODS, AND SURFACE-FREE ANALYSIS ON IMAGING DATA

In this section, we demonstrate the validity, accuracy and convergence properties of the diffuse Nitsche formulations discussed above with numerical benchmark problems in one, two and three dimensions. We also outline an effective workflow based on the diffuse Nitsche formulation

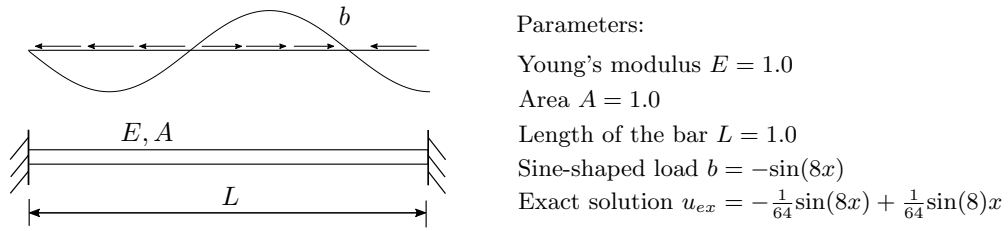


Figure 10: Uni-axial bar example with Dirichlet constraints at both ends.

that eliminates surface reconstruction for complex geometries based on imaging data, which we illustrate by surface-free compression tests on patient-specific CT scans of human vertebrae.

We also compare the diffuse Nitsche method to a class of diffuse penalty-type methods [24] that are obtained from (21) and (22) by maintaining the stabilization terms, but omitting all other expressions associated with the boundary. The result is a geometrically diffuse formulation of the penalty method: Find u_h such that $B(u_h, v_h) = l(v_h)$ for all v_h , where

$$B(u_h, v_h) = \int_{\mathcal{K}} \nabla u_h \cdot \nabla v_h \phi \, d\Omega + \beta \int_{\mathcal{K}} u_h v_h |\nabla \phi| \, d\Omega \quad (58)$$

$$l(v_h) = \int_{\mathcal{K}} f v_h \phi \, d\Omega + \beta \int_{\mathcal{K}} g v_h |\nabla \phi| \, d\Omega \quad (59)$$

In this case, β plays the role of a penalty parameter. The suitable choice of this parameter is crucial for the accuracy of any method based on (58) and (59) [24, 77, 78].

5.1. One-dimensional bar

We first illustrate the accuracy and convergence properties for the diffuse Nitsche method with a simple one-dimensional example. To this end, we consider the bar shown in Fig. 10, fixed at both ends and loaded by a sine-shaped load. To obtain a diffuse geometry for this example, we use the analytical function (55), with the diffuse boundary position $a = 0.0$ at the left end of the bar. For an illustration of the phase-field, we refer to Figs. 3 and 4 in Section 2.3.

For the finite element discretization of the diffuse Nitsche method, we consider an embedding domain $\mathcal{K} = [-1.0, 1.0]$ such that the displacement constraint at the right end $x = 1.0$ can be imposed strongly. Using standard quadratic nodal elements, we discretize the variational form (21) and (22) that employ diffuse approximations for the boundary and volume integrals, and the variational form (23) and (24) that employ a diffuse approximation for the boundary, but uses the sharp definition of the volume. For comparison, we also discretize the standard Nitsche method (12) and (13) that employs sharp definitions for both the boundary and the volume. We note that with the parameters given in Fig. 10, the variational formulation of an elastic bar coincides with the variational forms for the Poisson problem discussed earlier. To ensure that phase-field quantities are integrated accurately, we increase the number of Gauss points in elements in the diffuse boundary region. We remove elements from the discretization, for which the phase-field stays below 10^{-6} in the complete element support.

Figure 11 plots the relative error in the L^2 norm and the H^1 semi-norm when the initial mesh is uniformly refined. Errors are computed with respect to the exact domain $\Omega = [0.0, 1.0]$. We observe that optimal rates of convergence are achieved with the standard Nitsche method. The

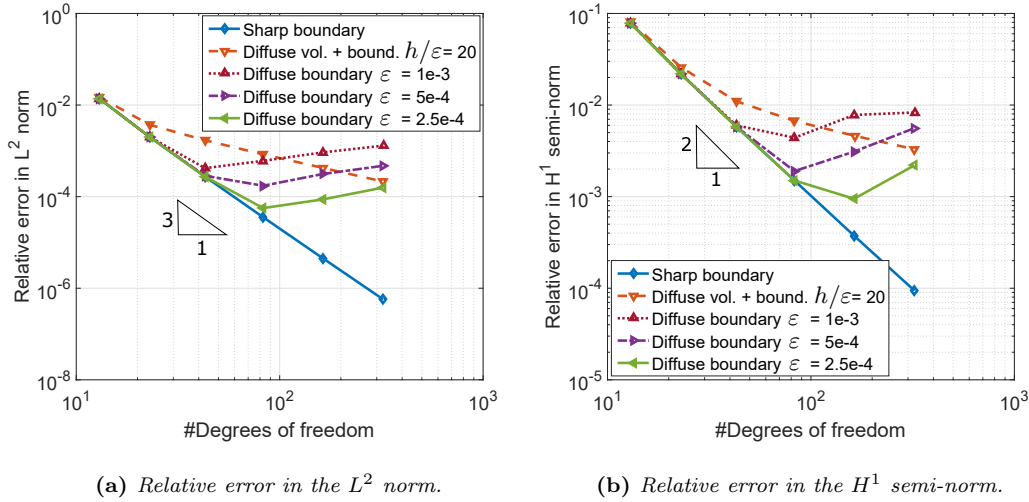


Figure 11: One-dimensional bar example: Convergence of error norms defined over the sharp domain for different sharp and diffuse Nitsche methods.

geometrically diffuse Nitsche formulation (21) and (22) with an initial length scale $\varepsilon_0 = 0.01$ yields suboptimal rates of convergence. When we tie the length scale of the phase-field to the mesh size with a constant ratio $\varepsilon/h = 1/20$, the overall accuracy is controlled by the phase-field, as the value of ε_0 is continuously bisected.

The diffuse Nitsche formulation (23) and (24) only imposes the boundary terms in a diffuse sense, but integrates all terms associated with the volume exactly. Figure 11 plots the corresponding convergence behavior for three different values of ε that are now held constant during mesh refinement. We observe that in this case, the diffuse formulation is able to achieve the same accuracy as a sharp boundary method in the pre-asymptotic range. The convergence curve levels off when the geometry error of the diffuse boundary becomes larger than the approximation error and therefore starts to dominate the total error. The curves plotted in Figs. 11a and 11b also demonstrate that the maximum accuracy directly correlates with the length-scale parameter ε used in the diffuse phase-field representation (55). We note that the same characteristic convergence behavior has been demonstrated for diffuse Neumann boundary conditions by NGUYEN and collaborators in [23].

We compare the accuracy of the diffuse Nitsche method with the diffuse penalty method (58) and (59), where we employ the variant with a diffuse boundary, but a sharp volume. We focus on an embedding mesh of 21 quadratic elements and the phase-field representation (55) with a length-scale parameter $\varepsilon = 0.0025$. Figure 12 shows the evolution of the error in the L^2 norm and the H^1 semi-norm, when we gradually increase the penalty parameter β from 1 to 10^{10} . We observe that there exist optimal values for the penalty parameter that minimize the error in each norm. These optimal penalty parameters, however, differ for each norm. The results also confirm that the error of the diffuse Nitsche method is of the same order of magnitude as the best possible results of the diffuse penalty method. Their stabilization parameters, however, have been automatically estimated as discussed in Section 3.2.

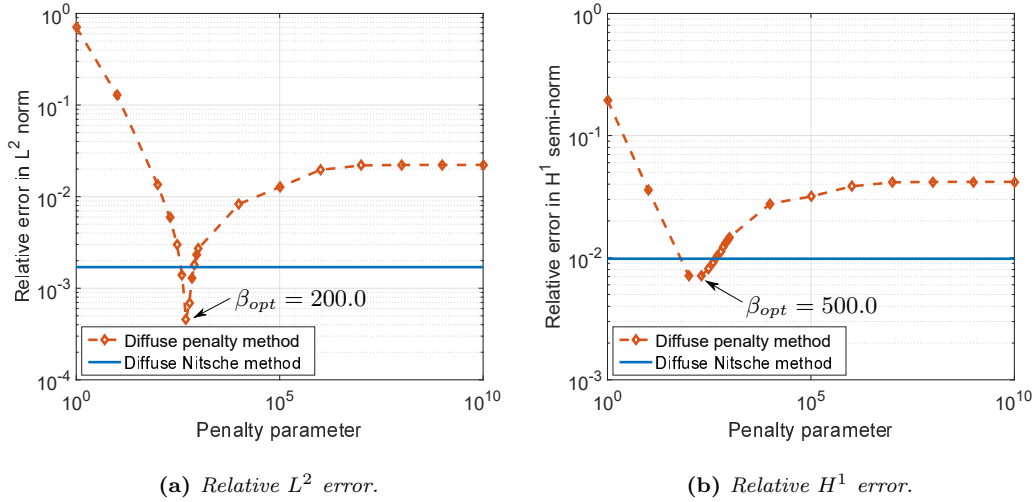


Figure 12: Accuracy of the diffuse penalty method for different values of the penalty parameter.

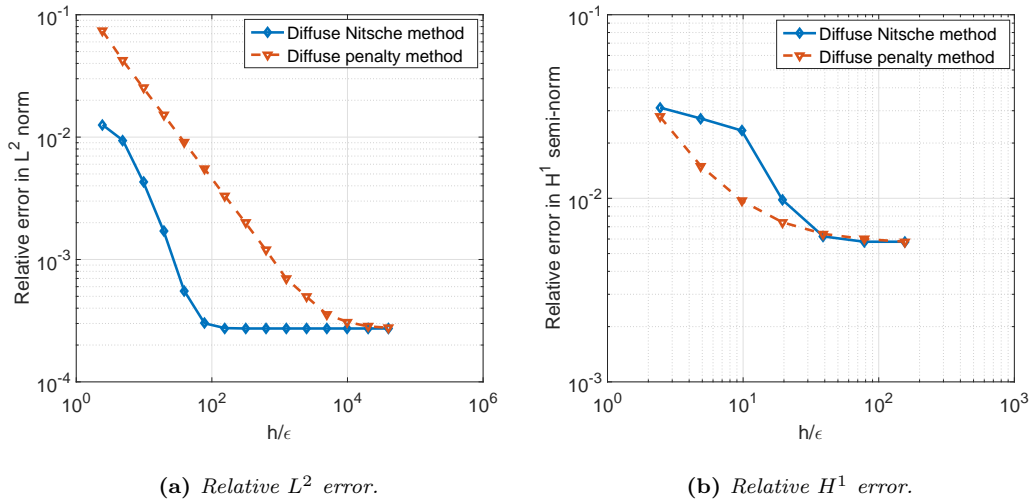


Figure 13: Convergence of the diffuse penalty method with $\beta = \varepsilon^{-3/4}$ and the diffuse Nitsche method on a mesh of 21 elements, when the length-scale parameter ε is gradually decreased.

Figure 13 plots the evolution of the L^2 and H^1 errors, when the length-scale parameter ε of the phase-field is gradually decreased on a 21 element mesh, increasing the ratio h/ε . For the diffuse penalty method, the penalty parameter is chosen as $\beta = \varepsilon^{-3/4}$, which provides the best possible convergence in the H^1 semi-norm [24, 78]. We observe that the diffuse Nitsche method with automatically estimated stabilization parameters achieves comparable accuracy in the H^1 semi-norm, but a significantly better convergence behavior in the L^2 norm. At a

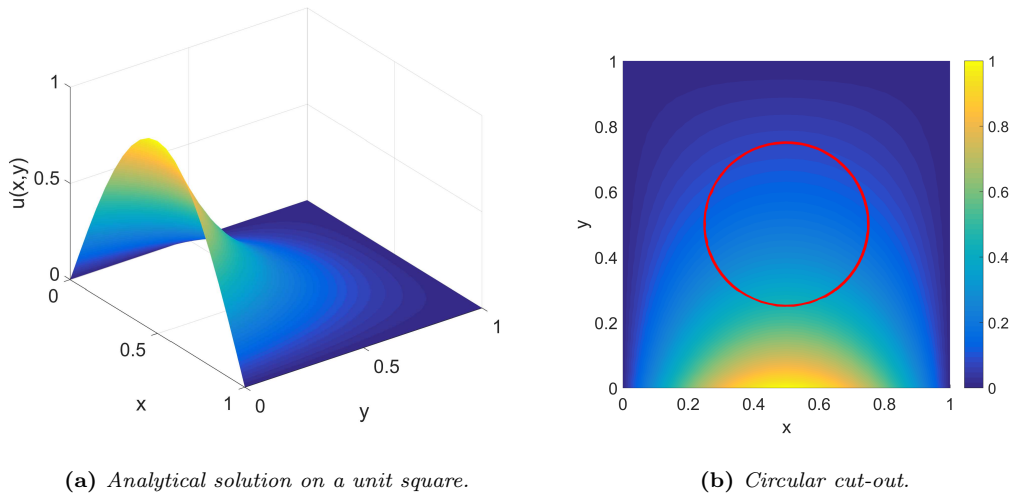


Figure 14: Analytical solution and domain definition for the two-dimensional Poisson problem.

certain level of h/ε , the approximation error of the 21 element mesh starts to dominate, and the error stops converging. To achieve the same final error level in the L^2 norm, the diffuse penalty method needs a length scale that is approx. 100 times smaller compared to the diffuse Nitsche method. If the phase-field needs to be computed as the solution of an initial boundary value problem, this leads to a significant increase in computational cost due to the much finer mesh size required to resolve the phase-field gradient in the diffuse boundary region.

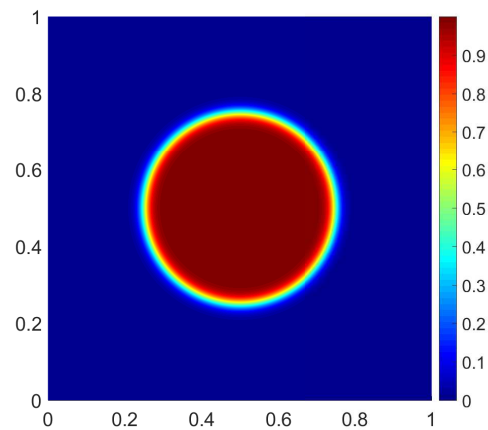
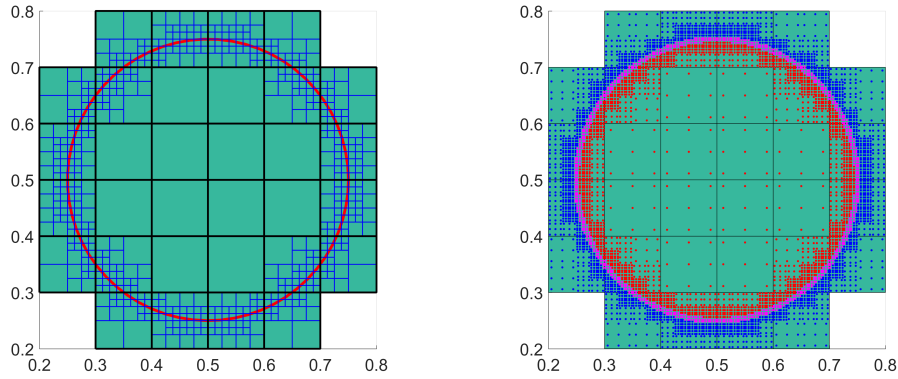


Figure 15: Diffuse representation of the circular disk with $\varepsilon = 0.02$, plotted on $\mathcal{K} = [0, 1]^2$.



(a) Structured grid (in black) with adaptive sub-cells (in blue).

(b) Adaptive quadrature points inside (red), outside (blue) and in the diffuse boundary region (magenta).

Figure 16: Diffuse domain discretization with quadratic nodal elements.

5.2. Two-dimensional Laplace problem

In the next step, we examine the accuracy and convergence properties for the diffuse Nitsche method in the two-dimensional setting with a Laplace problem whose governing equation corresponds to the model problem (1) with zero source term f . The original sharp domain Ω is a circular disk with diameter $d = 0.5$ and center point $(x_c, y_c) = (0.5, 0.5)$, on which the exact solution is given as

$$u_{\text{ex}}(x, y) = [\cosh(\pi y) - \coth(\pi) \sinh(\pi y)] \sin(\pi x) \quad (60)$$

We note that (60) corresponds to the solution of a Laplace problem defined on an embedding unit square $[0, 1]^2$ with Dirichlet boundary conditions $u(x, 0) = \sin(\pi x)$ and $u(x, 1) = u(0, y) = u(1, y) = 0$ [50]. Figure 14 illustrates the corresponding exact field on the unit square and on the circular domain. To obtain a finite element approximation of (60) on the disk, we impose Dirichlet boundary conditions given by (60) along the circular boundary.

For finite element discretizations in a diffuse domain context, we consider the embedding domain $\mathcal{K} = [0, 1]^2$. For the circular disk, we can easily construct a signed distance function, which we can use in (56) to obtain an analytical phase-field representation of the disk. Figure 15 illustrates the resulting phase-field for a length-scale parameter $\varepsilon = 0.02$. We discretize the variational forms of the two diffuse Nitsche variants, the diffuse penalty method and the standard Nitsche method with structured grids of standard quadratic nodal elements. We remove elements from the discretization, for which the phase-field stays below 10^{-3} in the complete support. To ensure that phase-field quantities are integrated accurately, we employ the adaptive quadrature strategy discussed in Section 4.4 for elements with support in the diffuse boundary region. The sub-cell structure aggregates quadrature points in the diffuse boundary region, which is illustrated for an example mesh in Fig. 16.

Figure 17 plots the relative error in the L^2 norm and the H^1 semi-norm under uniform mesh refinement, where errors are evaluated on the sharp disk. Optimal rates of convergence

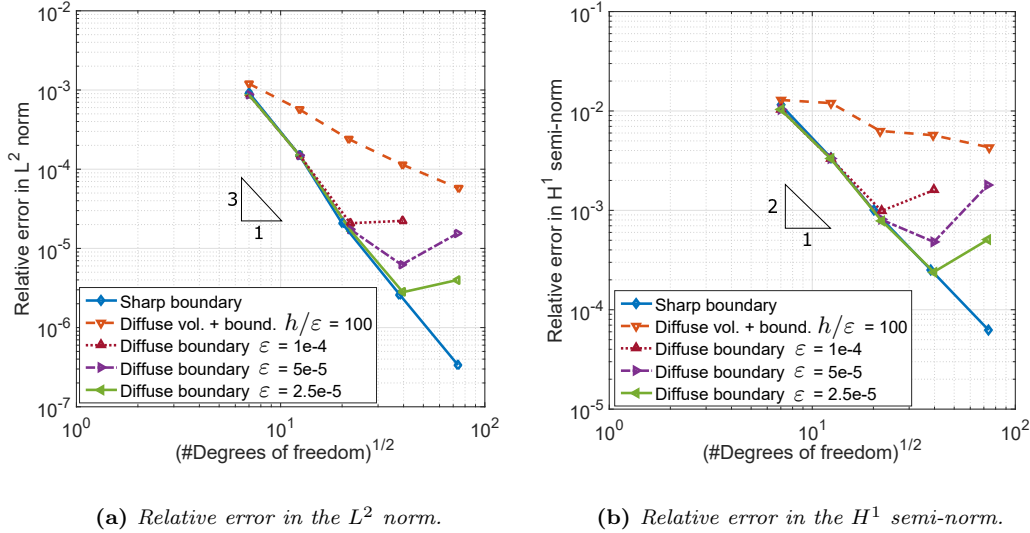


Figure 17: 2D Laplace example: Convergence of error norms defined over the sharp disk for different sharp and diffuse Nitsche methods.

are confirmed for the standard Nitsche method that uses geometrically sharp definitions. The geometrically diffuse Nitsche formulation (21) and (22) with an initial length scale $\varepsilon_0 = 0.002$ yields the same suboptimal rates of convergence as for the 1D bar above, when we tie the characteristic length scale of the phase-field to the mesh size ($\varepsilon/h = 1/100$). We show convergence for the diffuse Nitsche formulation (23) and (24) that integrates only terms associated with the boundary in a diffuse sense for three different values of ε that are held constant during mesh refinement. We observe again that in the pre-asymptotic range, the diffuse formulation is able to achieve the same accuracy as the standard Nitsche method.

We also compare the accuracy of the diffuse Nitsche method (23) and (24) with the diffuse penalty method (58) and (59). We employ the same embedding mesh of 6×6 quadratic elements and a phase-field with $\varepsilon = 0.0001$. Figure 18 shows the evolution of the error in the L^2 norm and the H^1 semi-norm, when we gradually increase the penalty parameter β from 1 to 10^{10} . We notice again two different optimal values of the penalty parameter that minimize the error in each norm. The plots also confirm that the diffuse Nitsche method with automatically estimated element-wise stabilization parameters leads to errors that are equivalent to the best possible case in the diffuse penalty method.

Figure 19 plots the evolution of the L^2 and H^1 errors on the 6×6 mesh, when ε is gradually decreased. For the diffuse penalty method, the penalty parameter is again chosen as $\beta = \varepsilon^{-3/4}$ [24]. We observe that the diffuse Nitsche method shows a considerably better convergence rate, so that it achieves any given error level at a significantly larger length scale of the phase-field than the diffuse penalty method. For example, to reach the minimum L^2 error with the given ε , the diffuse penalty method requires an approx. 1,000 times smaller length-scale parameter than the diffuse Nitsche method, leading to a considerable increase in mesh size and hence

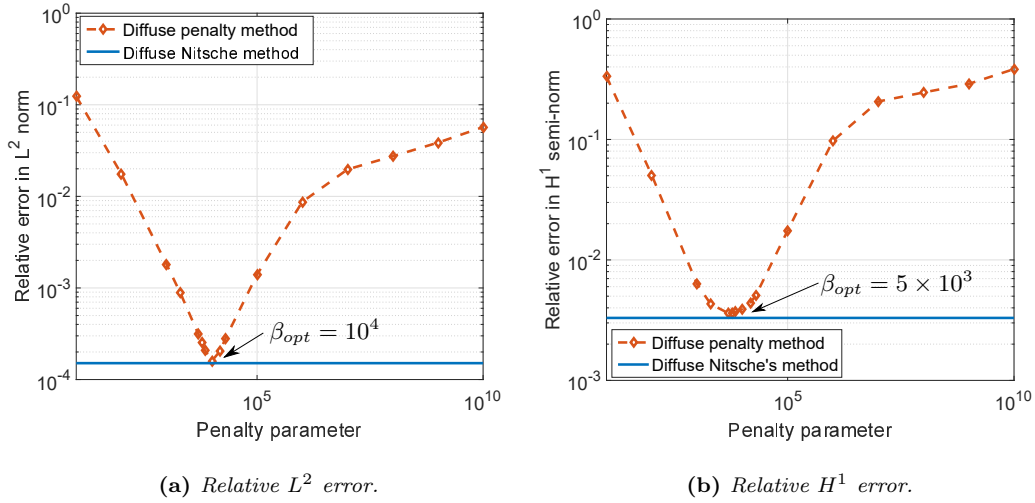


Figure 18: 2D Laplace example: Accuracy of the diffuse penalty method for different values of the penalty parameter.

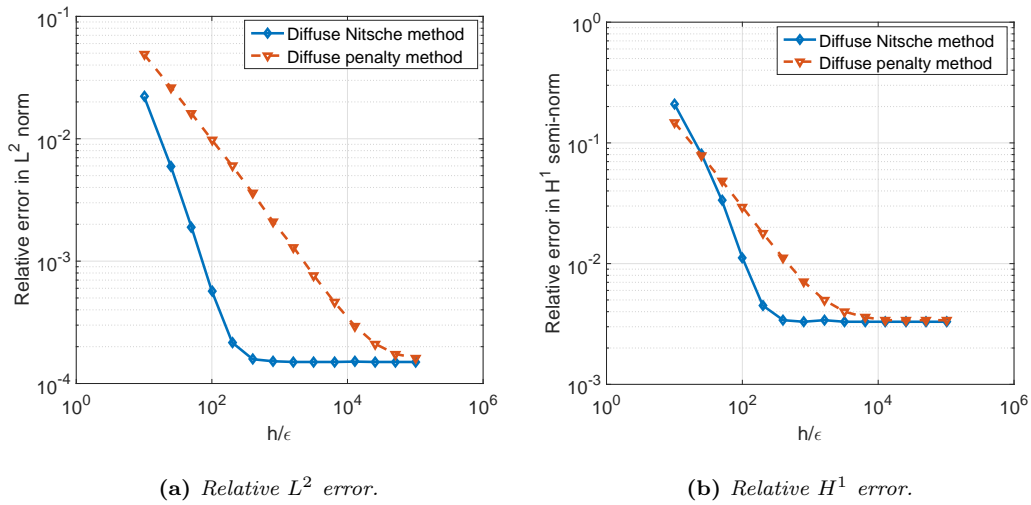


Figure 19: 2D Laplace example: Convergence of the diffuse penalty method ($\beta = \epsilon^{3/4}$) and the diffuse Nitsche method on a 6×6 mesh, when the length-scale parameter ϵ is gradually decreased.

computational cost for the solution of an associated phase-field boundary value problem.

In each element with support on the diffuse boundary, the diffuse Nitsche method uses the local eigenvalue problem (45). The largest eigenvalue represents an estimate for the minimum value of the stabilization parameter β that ensures stability. Figure 20 shows element-wise estimates of β for two example meshes. We observe that the difference in the absolute value

for β varies significantly as smaller cut elements require a larger stabilization parameter. This behavior is in line with the behavior of local stabilization parameters in the standard Nitsche method based on sharp boundary and volume definitions (see, e.g., [62]).

Figures 21 and 22 plot the relative error distribution for the solution and its derivatives, respectively, when the length scale ε of the diffuse boundary region is gradually decreased on a fixed 6×6 mesh of quadratic elements. The error distributions are computed as

$$e(x, y) = \frac{|w_{\text{num}} - w_{\text{ex}}|}{|w_{\text{ex}}|} \quad (61)$$

for any field w , computed numerically and taken from an exact reference. We observe that for practical values of h/ε , the error is significant at the diffuse boundary, where the solution is not accurately defined. In the bulk of the domain away from the diffuse boundary region, however, the error is small, even for large h/ε . We also observe that if we reduce h/ε to (impractically) small values, both the solution and its derivatives converge to the same error distributions that is obtained with the standard Nitsche method based on the sharply defined geometry.

5.3. Three-dimensional spherical thick shell

To illustrate accuracy and convergence of the diffuse Nitsche method in three dimensions, we consider the spherical thick shell in Fig. 23. We assume inner and outer radii $R_i = 50$ and $R_a = 100$, Young's modulus $E = 10,000$, Poisson ratio $\nu = 0.3$, a traction-free outer shell surface and a radial displacement $u_r = 0.2$ on the inner shell surface. Due to symmetry, we consider only one eighth of the problem. There exists an analytical solution [79, 80] in spherical coordinates $\{r, \phi, \theta\}$ that yields the exact strain energy $U_{ex} = 157,079.6326794896$.

For the geometric description of its volume, we consider either the sharp boundary representation shown in Fig. 23 or a corresponding voxel model. The voxel model describes the volume of the sphere implicitly by local material information associated with each voxel. If located inside the sphere, a voxel holds Young's modulus $E = 10,000$, otherwise Young's

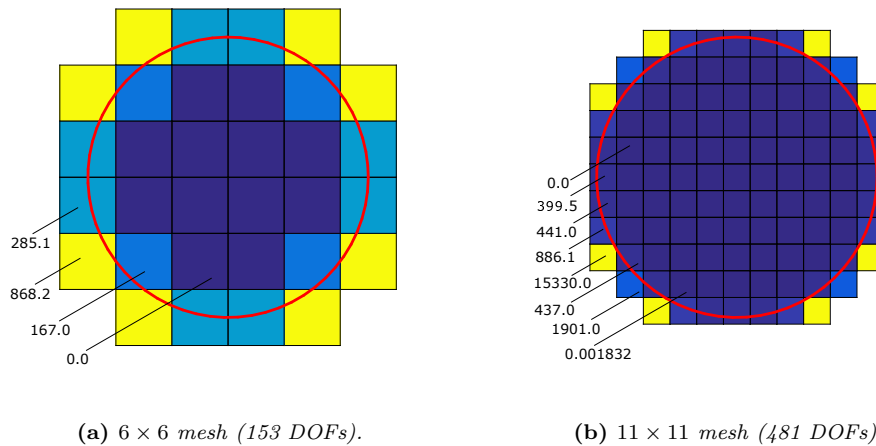


Figure 20: 2D Laplace example: Element-wise stabilization parameters estimated from the local eigenvalue problem (the red circle is the center line of the diffuse boundary with length scale $\varepsilon = 10^{-3}$).

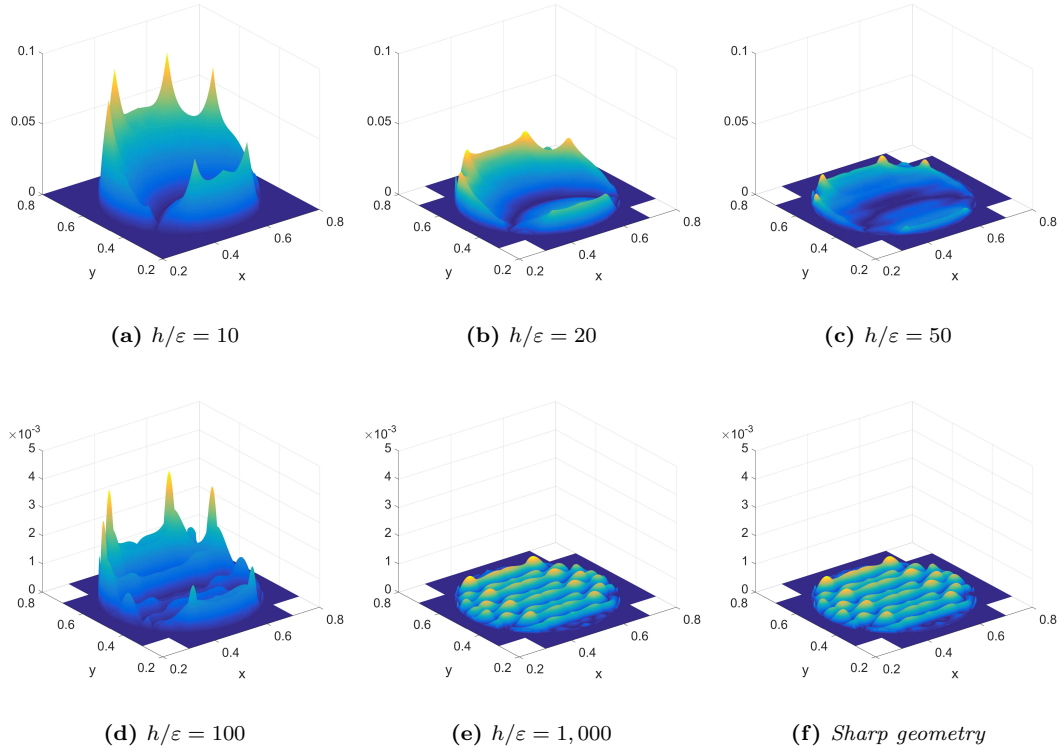


Figure 21: Relative error distribution of the solution field obtained on a 6×6 mesh with the diffuse Nitsche method at different ε and the standard Nitsche method (sharp geometry).

modulus is zero. Figure 24 plots all voxels with non-zero Young's modulus, omitting those with no stiffness. The resolution of the voxel model is characterized by a length scale Δ associated with the grid spacing. For the evaluation of volume integrals based on voxels, the concept of intersected elements does not apply, as there exists no sharply defined boundary of the domain. Instead, we follow the quadrature principles outlined in [23, 57, 75]. First, tetrahedral elements for which all voxels show zero stiffness, are removed from the mesh. Second, we subdivide all remaining elements into sub-cells. The sub-cell resolution is chosen such that the density of the resulting quadrature points sufficiently reflects the stiffness variation of the voxel model.

While the symmetry boundary conditions along straight boundaries can be imposed strongly and the traction-free Neumann boundary conditions at the outer shell surface do not require integration, the Dirichlet boundary conditions at the inner spherical boundary are imposed weakly. For the geometric description of the inner surface, we consider either a sharp surface given by a very fine tessellation or the gradient of a diffuse phase-field function, generated analytically from (56) with a suitable signed distance function. Figure 25 illustrates both surface representations.

In the first step, we employ the variant of the diffuse Nitsche method that uses the sharp representation of the domain to evaluate all terms associated with the volume. Following the

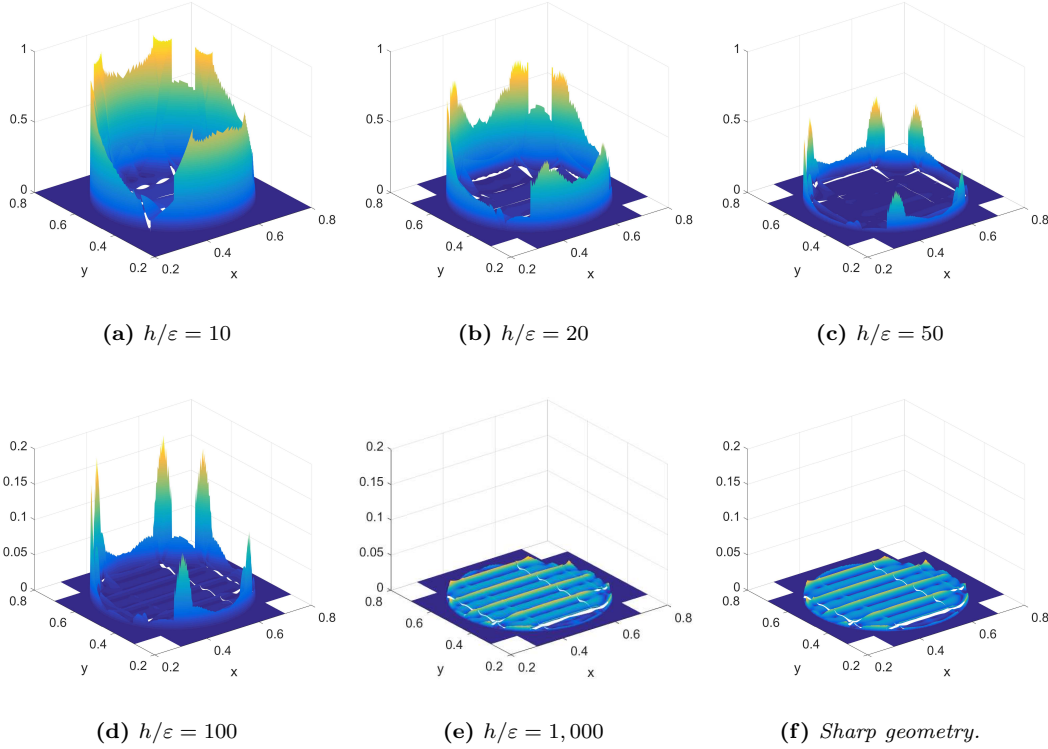


Figure 22: Relative error distribution of the norm of the solution gradient, obtained on a 6×6 mesh with the diffuse Nitsche method at different ε and the standard Nitsche method (sharp geometry).

steps shown in Section 2, we can derive the variational formulation for linear elasticity: Find the displacement field \mathbf{u} such that $B(\mathbf{u}, \delta \mathbf{u}) = l(\delta \mathbf{u})$ for all $\delta \mathbf{u}$, where

$$B(\mathbf{u}, \delta \mathbf{u}) = \int_{\Omega} \boldsymbol{\sigma} : \delta \boldsymbol{\varepsilon} \, d\Omega + \int_{\mathcal{K}} \mathbf{u} \cdot (\delta \boldsymbol{\sigma} \cdot \nabla c) \, d\Omega + \int_{\mathcal{K}} (\boldsymbol{\sigma} \cdot \nabla c) \cdot \delta \mathbf{u} \, d\Omega + \beta \int_{\mathcal{K}} \mathbf{u} \cdot \delta \mathbf{u} \, |\nabla c| \, d\Omega \quad (62)$$

$$l(\delta \mathbf{u}) = \int_{\Omega} \mathbf{b} \cdot \delta \mathbf{u} \, d\Omega + \int_{\mathcal{K}} \hat{\mathbf{u}} \cdot (\delta \boldsymbol{\sigma} \cdot \nabla c) \, d\Omega + \beta \int_{\mathcal{K}} \hat{\mathbf{u}} \cdot \delta \mathbf{u} \, |\nabla c| \, d\Omega \quad (63)$$

and $\boldsymbol{\sigma}$, $\delta \mathbf{u}$ and $\delta \boldsymbol{\varepsilon}$ denote the stress tensor, the virtual displacement vector and the virtual strain tensor, respectively. We recall that Ω represents a sharp representation of the domain and \mathcal{K} an embedding domain that contains the diffuse boundary region. Each component of the given displacement vector $\hat{\mathbf{u}}$, initially defined on the sharp Dirichlet surface Γ_D , is extended along the surface normal such that it is well-defined over the complete diffuse boundary region [5]. We note that the automatic estimation procedure for the stabilization parameter based on a local eigenvalue problem can be directly extended to (62) and (63) (see, e.g., [62]).

Figure 26a illustrates the initial unfitted finite element mesh of quadratic tetrahedral

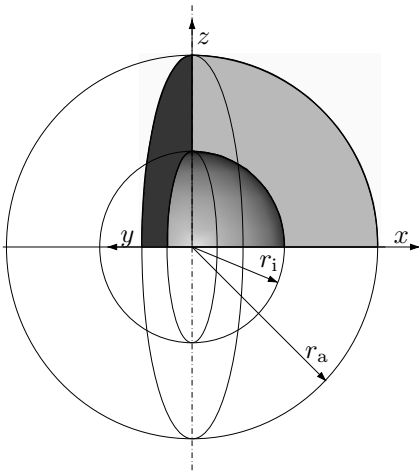


Figure 23: A thick spherical shell.

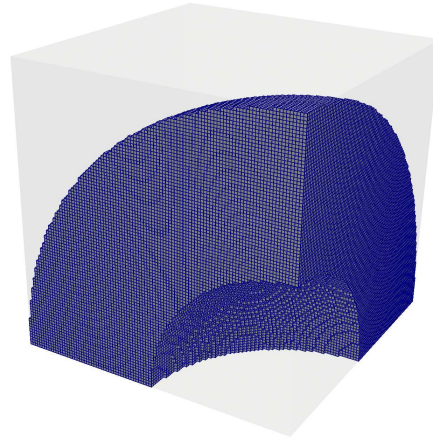


Figure 24: Voxel model ($\Delta = 1$).

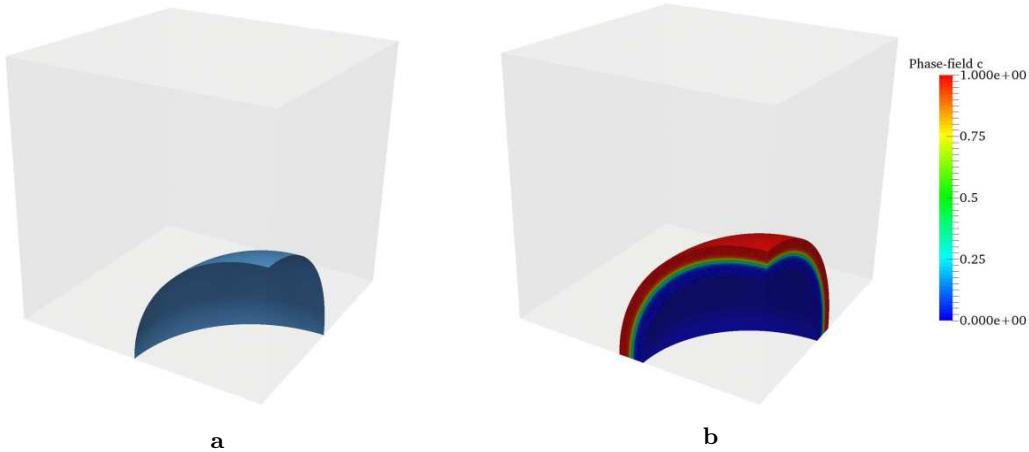
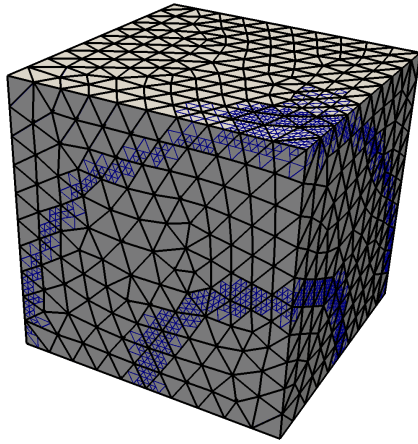


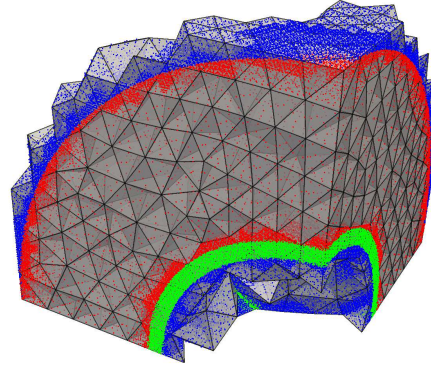
Figure 25: Geometric description of the inner surface: (a) sharp (very fine tessellation), (b) diffuse (phase-field of length scale $\varepsilon = 1.0$).

elements generated for the embedding cube. We subsequently remove all elements, for which the phase-field stays below 10^{-3} in the element support. Figure 26b illustrates the adaptive quadrature strategy discussed in Section 4.4 that ensures the accurate integration of phase-field quantities in the diffuse boundary region.

We monitor the accuracy of diffuse Dirichlet boundary conditions by measuring the strain energy error defined over the sharp volume. Figure 27a plots the relative error under mesh refinement. We observe that the standard Nitsche method enables optimal convergence in the complete accuracy range. The diffuse variant of Nitsche's method enables optimal convergence rates in the pre-asymptotic range, but convergence stops at a critical error level controlled by the length-scale parameter ε of the phase-field. These results confirm the characteristic

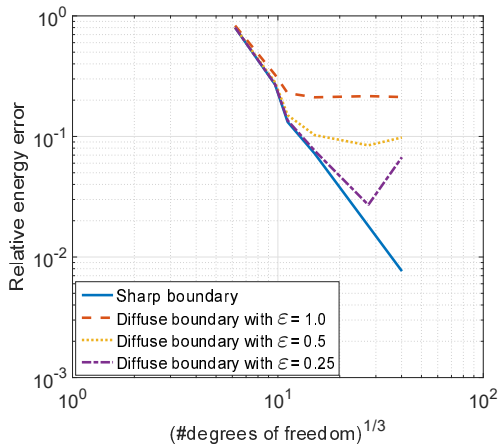


(a) Tetrahedral mesh of the complete embedding domain (black) and adaptive quadrature sub-cells (blue).

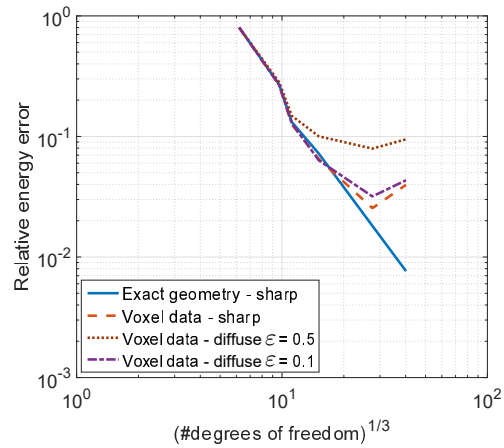


(b) Quadrature points inside (red), outside (blue) and in the diffuse boundary region (green).

Figure 26: Embedded domain meshing, element removal and adaptive quadrature for the spherical thick shell example. Note that the diffuse Nitsche method is employed only at the inner shell surface.



(a) Sharp representation of the volume with different sharp/diffuse boundary representations.



(b) Voxel representation of the volume with different sharp/diffuse boundary representations.

Figure 27: Spherical thick shell example: Convergence of the relative error in strain energy for different variants of diffuse and sharp Nitsche methods.

convergence behavior demonstrated in one and two dimensions.

In the second step, we perform numerical integration of all terms associated with the volume with voxel quadrature, based on the model shown in Fig. 24. To this end, we replace all sharp

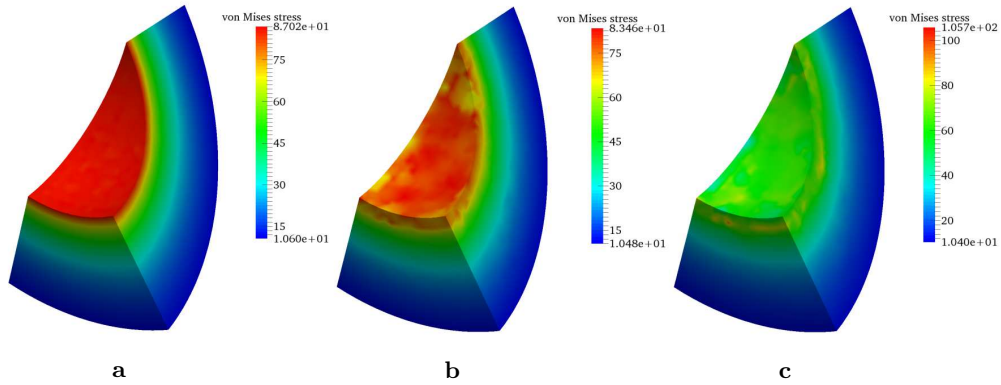
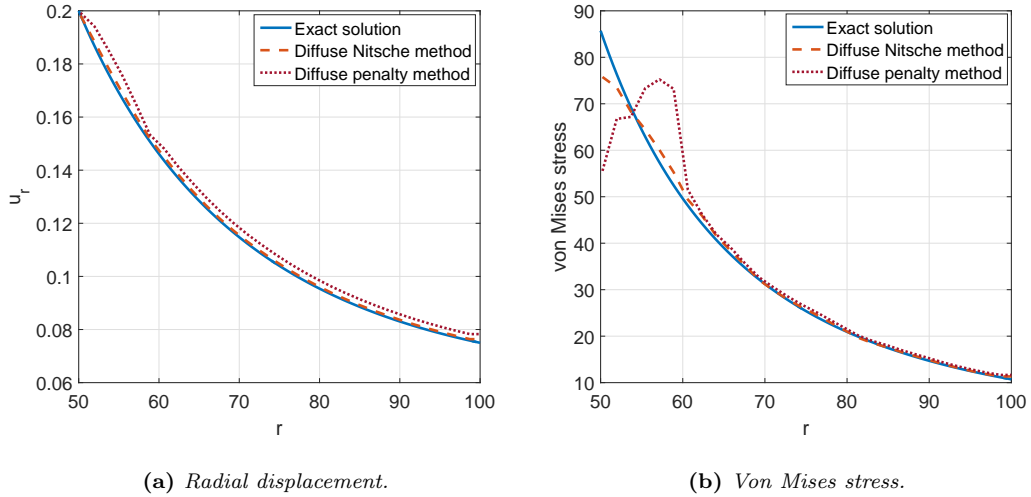


Figure 28: *von Mises stress plotted over a section of the spherical thick shell: (a) Exact solution, (b) diffuse Nitsche method, (c) diffuse penalty method. The diffuse methods use a phase-field approximation of the inner boundary with $\varepsilon = 0.25$.*



(a) *Radial displacement.*

(b) *Von Mises stress.*

Figure 29: *Solution fields plotted along an arbitrary cut line in radial direction. The diffuse Nitsche method and the diffuse penalty method both use the mesh shown in Fig. 26.*

volume integrals by voxel integrals as follows

$$\int_{\Omega} Q \, d\Omega \approx \int_{\Omega_{\text{vox}}} Q \, d\Omega \quad (64)$$

where Ω_{vox} denotes the rasterized voxel representation that approximates the sharp domain Ω by all voxels with non-zero Young's modulus. Figure 27b plots the corresponding relative error in strain energy under uniform mesh refinement. We observe that convergence stops at a critical accuracy level, also for the standard Nitsche method that uses a sharp boundary surface. It can be shown, see for example the discussion in Section 3 in [42], that the reason is the limited voxel resolution and the associated quadrature error. Of particular interest

from an engineering point of view is the pre-asymptotic range, where standard and diffuse Nitsche methods achieve optimal rates of convergence at exactly the same accuracy level. This observation suggests that the diffuse Nitsche method with voxel quadrature and a properly chosen length scale ε is able to achieve exactly the same accuracy and convergence behavior as the standard Nitsche method with voxel quadrature and sharply defined surfaces.

We also compare the accuracy of the diffuse Nitsche method with a corresponding diffuse penalty method that is obtained from (62) and (63) by dropping the Nitsche terms, but maintaining the stabilization terms, where β is now a penalty parameter. Both diffuse methods employ the mesh shown in Fig. 26 and the length-scale parameter $\varepsilon = 0.25$ for the phase-field approximation of the boundary. The diffuse Nitsche method estimates stabilization parameters automatically from a local eigenvalue problem, while the diffuse penalty method uses an empirically chosen penalty parameter $\beta = 1,000 \times E$. Figure 28 compares the analytical von Mises stress to the von Mises stress computed with the diffuse Nitsche method and the diffuse penalty method for a section of the thick shell. Figure 29 compares the same three fields plotted along a radial cut line. For displacements, both diffuse methods achieve accurate results, also close to the diffuse boundary region, where the diffuse Nitsche method is slightly better. For stresses, the plots demonstrate that in the bulk of the domain, the solution fields achieve a comparable accuracy irrespective of the diffuse method used. The stress accuracy close to the diffuse boundary region, however, varies greatly, with a significant advantage for the diffuse Nitsche method. While both methods are not accurate in the diffuse boundary region, the diffuse Nitsche method leads to significantly smaller deviations from the analytical solution and its area of influence of the diffuse boundary region is considerably smaller than in the diffuse penalty method.

5.4. Relating phase-field length scale, voxel spacing and mesh size

Both the voxel model and the diffuse phase-field model are characterized by length-scale parameters: the voxel spacing, Δ , and the phase-field parameter, ε . The mesh size, h , that controls the accuracy of the finite element approximation of the physics-based solution represents an additional length scale parameter. The success of the diffuse Nitsche method depends on a suitable relation between the three length scales involved.

We observe in Figs. 27a and 27b that if we properly relate the two length scale parameters Δ and ε , the convergence curves obtained with the diffuse Nitsche method that uses sharp volume quadrature and the diffuse Nitsche method that uses voxel quadrature level off at approximately the same critical point. According to our numerical tests, $\varepsilon = 0.5 \Delta$ is a good choice. Figures 27a and 27b also show that the strain energy error might increase again when the mesh size has passed the critical point. Our observations indicate that the reason for this phenomenon are spurious stress oscillations in the diffuse boundary region. They start to appear when the mesh size is small enough to resolve the physics-based solution in the part of the diffuse boundary region where voxels have no stiffness. From a practical viewpoint, it is therefore important to bound the minimum mesh size h in terms of ε . Our numerical tests indicate that for quadratic basis functions, $h > 10\varepsilon$ is a reliable lower bound for the mesh size that ensures that stress oscillations do not occur. Therefore, we can summarize a desirable relation between the three inherent length scales as follows

$$h \gtrsim 10\varepsilon \approx 5\Delta \quad (65)$$

The constraint on the mesh size h by the voxel spacing Δ in (65) that automatically follows

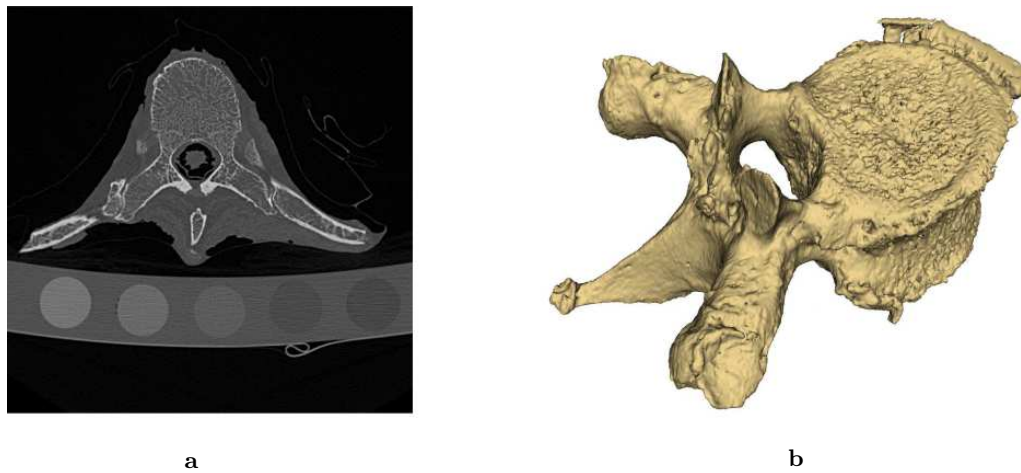


Figure 30: Human vertebra: (a) slice of the original CT scan, (b) voxel model of the segmented vertebra

from the above considerations is in line with the limitation that the accuracy of finite element schemes based on voxel quadrature cannot be increased by mesh refinement beyond the voxel resolution [23, 65, 75].

5.5. Stress analysis of a patient-specific vertebra

We finally demonstrate the strength of the diffuse Nitsche method for the analysis of complex geometries based on imaging data. Adapting the vertebra example from [23], we apply the diffuse Nitsche formulation for conducting a displacement-driven compression test. Due to their complicated geometry, creating an explicit parametrization of the loading and support surfaces at the upper and lower faces of the vertebra constitutes a significant challenge for the automation of simulation workflows. The geometric basis of the structure is again an implicit voxel model that has been derived from CT scans as described in [23] and illustrated in Fig. 30. The voxel spacing is $\Delta_x = \Delta_y = 0.1465$ mm and $\Delta_z = 0.3$ mm. The vertebra is separated from the surrounding bone structures with the help of the open-source image processing library ITK (<https://itk.org/>). For each voxel in the vertebra, we assume the following material parameters: Young's modulus $E = 10$ GPa, Poisson's ratio $\nu = 0.3$ [81].

We employ the procedure based on the Allen-Cahn equation to determine a phase-field description ϕ of the implicit voxel model. To minimize computational cost, we solve the Allen-Cahn problem on two embedding rectangular domains that contain only the boundary region instead of the complete vertebral body (see illustration in Fig. 31a for the upper face). We then define a stiffness threshold that specifies the distinction between the physical domain Ω of interest and the rest of the domain outside. This yields an initial condition at each voxel, with which we can solve the Allen-Cahn problem (51) through (54) on a suitable mesh that is adaptively refined at all voxels close to the threshold such that the local element size h corresponds to the characteristic length scale ε of the Allen-Cahn problem. We choose the length scale of the phase-field as $\varepsilon = 0.15$ mm, one half of the largest voxel spacing, and discretize the rectangular domain with linear tetrahedral elements of finest mesh size

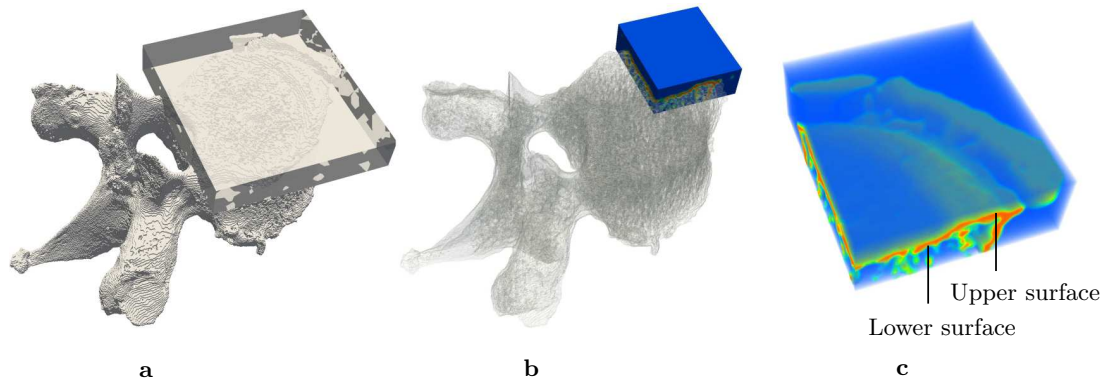
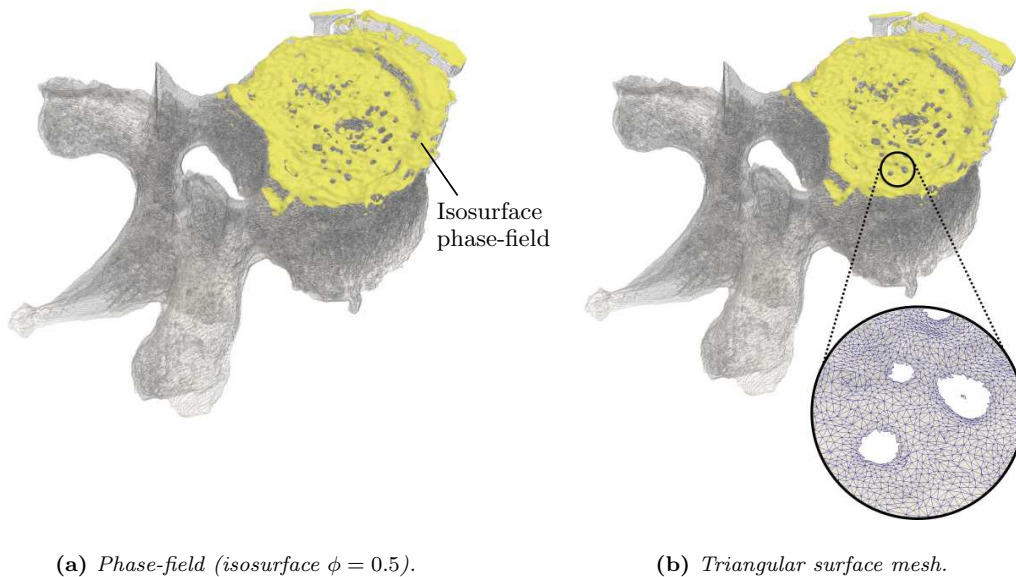


Figure 31: Diffuse representation of the upper surface: (a) domain for computing the Allen-Cahn problem, (b) and (c) part of the phase-field solution



(a) Phase-field (isosurface $\phi = 0.5$).

(b) Triangular surface mesh.

Figure 32: Diffuse implicit vs. sharp explicit representation of the upper cortical shell surface.

$h = 0.1$ mm. Figure 31b and 31c illustrate the resulting phase-field representation of the upper surface of the vertebra. To be able to compare accuracy with the standard Nitsche method, we also manufacture a corresponding explicit surface representation by transferring the phase-field isosurface at $\phi = 0.5$ into a tessellation composed of approx. 13,000 triangular facets. The outward surfaces of the upper cortical shell parametrized implicitly by the phase-field and explicitly by the tessellation are illustrated in Figs. 32a and 32b, respectively. We compute a second phase-field representation and explicit tessellation for the lower boundary region of the vertebra in the same way.

Since we are particularly interested in the strength of the vertebral body that carries the

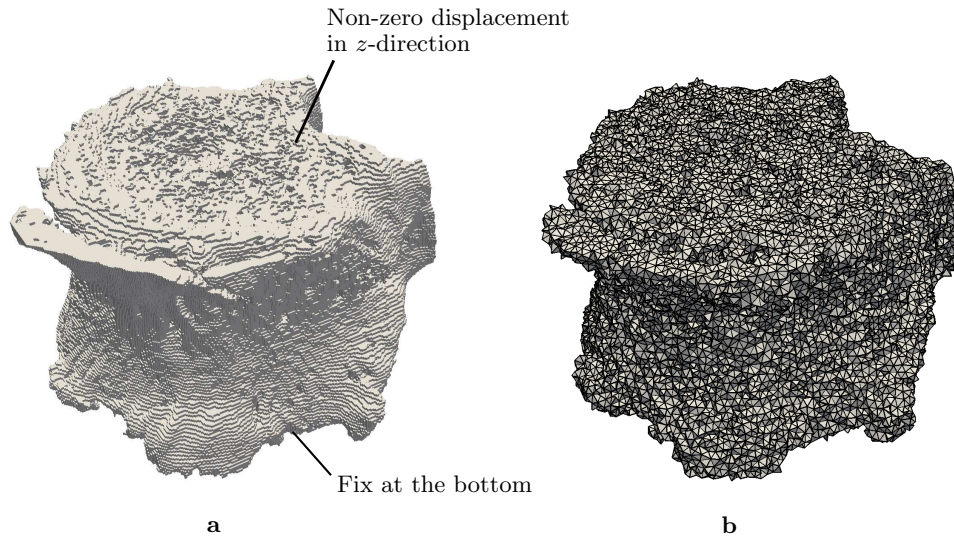


Figure 33: Full vertebra: (a) Voxel model and boundary conditions, (b) unfitted finite element mesh

bulk of the load, we cut away the vertebral arch, leading to the voxel model in Fig. 33a. We discretize the structure with an unfitted quadratic tetrahedral mesh shown in Fig. 33b, which consists of 494,151 nodes and 1,482,453 degrees of freedom. Using the diffuse Nitsche method with voxel quadrature and automatically estimated stabilization parameters, we impose a vertical displacement of $u_z = 1\text{mm}$ at the outward phase-field surface of the upper cortical shell and support the structure at the outward phase-field surface of the lower cortical shell. For comparison, we also apply the standard Nitsche method on the same discretization with tessellations of the upper and lower surfaces to impose displacements in a sharp sense.

Remark 3: We can observe in Fig. 31c that the phase-field resolves both the upper and lower side of the cortical shell. To distinguish between the two sides, we monitor the normal vector of the diffuse surface (19) at each quadrature point. Its contribution to the diffuse boundary terms only if the vertical component of the normal vector is within the range $n_z \geq 0.8$. This constitutes an effective way to prevent that parts of the surface are taken into account that correspond to the lower side of the cortical shell and to horizontal surfaces at the lateral sides of the vertebra. At the bottom surface, only quadrature points, for which the vertical component of the phase-field normal vector (19) lies within $n_z \leq -0.8$, are taken into account.

Figures 34 and 35 plot the total displacements and the von Mises stress, including zooms of part of the trabecular region, both obtained with the diffuse Nitsche method. Figure 36 plots the von Mises stress obtained with the standard Nitsche method and geometrically sharp boundary representations. We observe that the stress solutions in Figs. 35 and 36 match very well. In particular, the zoom areas indicate that the stress pattern obtained with the diffuse and sharp Nitsche variants agree very well both qualitatively and quantitatively.

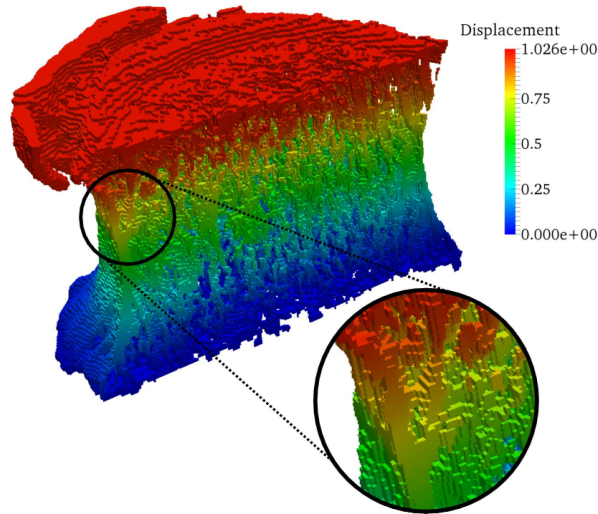


Figure 34: *Compression test of a vertebra: total displacements obtained with the diffuse Nitsche method.*

6. SUMMARY, CONCLUSIONS AND OUTLOOK

In this paper, we explored diffuse formulations of Nitsche’s method for imposing Dirichlet boundary conditions on phase-field approximations of sharp domains. The method is based on a phase-field that represents the domain and its boundary in a diffuse sense. We discussed the approximation of the Dirac distribution at the sharp boundary by the phase-field gradient in the diffuse boundary region that enables the transfer of sharp surface integrals at the boundary into diffuse volumetric integrals. We argued that for consistency, the phase-field approximation of the Dirac distribution needs to replicate the property that its integration across the diffuse boundary region yields one. Applying this concept to the boundary integrals in the classical variational formulation of Nitsche’s method, we arrived at a diffuse format of Nitsche’s method. We put particular emphasis on a variant that maintains sharp integrals for all terms associated with the volume of the domain, but uses the diffuse concept to transfer all boundary integrals into volumetric source terms, thus completely eliminating the need for explicit boundary parametrizations. This is of particular relevance for the analysis of image-based geometries, where volume integrals can be naturally integrated in a sharp sense by voxel quadrature schemes, but sharp boundary integrals require time-consuming and error-prone segmentation and surface reconstruction procedures.

In the next step, we stated conditions for the stability of the discrete system and generalized the automatic estimation of the stabilization parameter from a local eigenvalue problem to the diffuse setting. We observed that element-wise estimated stabilization parameters are significantly larger in elements that have only small support in the diffuse boundary region, which is equivalent to the behavior of stabilization parameters for elements with small cuts in the standard sharp Nitsche method. In this context, we also discussed the treatment of elements that have a small support in the diffuse boundary region, but no support in the sharp volume. We showed that this requires an additional stabilization parameter in the volume

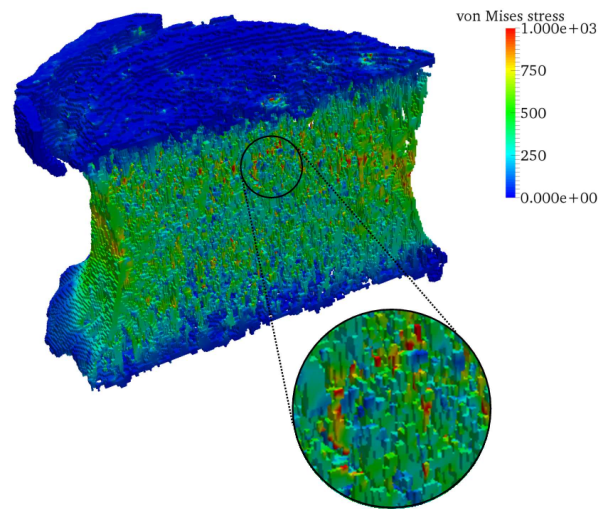


Figure 35: *Compression test of a vertebra: von Mises stress obtained with the diffuse Nitsche method.*

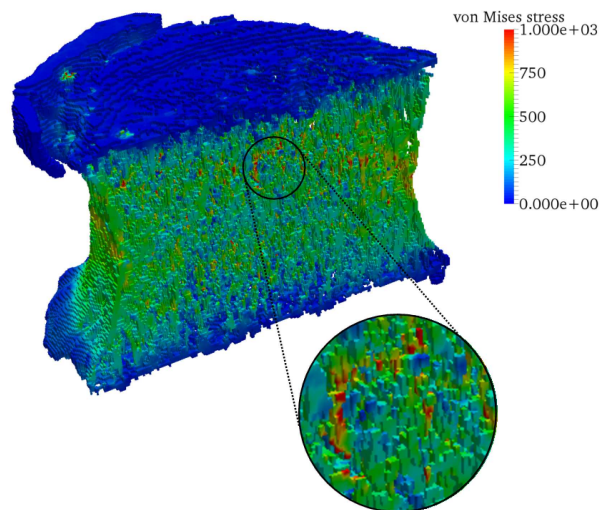


Figure 36: *Compression test of a vertebra: von Mises stress obtained with the standard Nitsche method based on explicit tessellations of the top and bottom surfaces.*

parametrization to avoid singularity of the local eigenvalue problem.

The diffuse Nitsche method relies on the availability of a suitable diffuse geometry model. We presented the construction of phase-field approximations of sharp domains from the short-term dynamic solution of an initial boundary value problem based on the Allen-Cahn equation. The procedure is particularly suitable for imaging data such as CT scans, where an initial condition can be easily found at each voxel by defining a suitable threshold. In the case of imaging data, the phase-field is just another implicit representation of the geometry, but in

contrast to the voxel model allows the extraction of boundary information in terms of its gradient. Since the boundary in a voxel model is not determined sharply, the phase-field approximation corresponds to the “data reality” of the original image representation. Since for optimal accuracy, the length scale of the phase-field must be smaller than the mesh size in the physics-based solution, we also discussed the use of mixed meshes, where the phase-field solution can be represented by a mesh that is much finer than the mesh for discretizing the diffuse Nitsche formulation. This prevents an overkill in terms of unnecessary degrees of freedom in the physics-based solution, but requires adaptive quadrature schemes that are able to accurately integrate steep phase-field gradients in elements with support in the diffuse boundary region.

We conducted a series of numerical tests in one, two and three dimensions. On the one hand, the results showed that the diffuse Nitsche method leads to sub-optimal convergence, including a pronounced error in the diffuse boundary region. On the other hand, they also showed that in image-based simulations based on voxel geometries the diffuse Nitsche method achieves the same accuracy as the standard Nitsche method with sharply defined surfaces, if the characteristic length scale of the phase-field, ε , the voxel spacing of the imaging data and the mesh size of the finite element approximation are properly related. We found from our numerical tests that ε should be approximately one half the voxel size and that the mesh size must be larger than 10 times ε . We also demonstrated significant advantages of the diffuse Nitsche method over diffuse penalty-type methods, such as a significant increase in accuracy in terms of L^2 and H^1 errors, a considerably reduced area of influence of the diffuse boundary region, and the automatic estimation of suitable stabilization parameters that guarantee the best possible accuracy. Adapting the example of a human vertebra based on patient-specific CT scans from NGUYEN et al. [23], we outlined a simplified workflow that eliminates the time-intensive manual identification of sharp boundary surfaces and their location within the thin cortical shell of a vertebral body. The simulation results of a compression test illustrated that the diffuse Nitsche method is able to handle extremely complicated surfaces and produces stress patterns that are almost indistinguishable from those computed with the standard Nitsche method and explicit tessellations of sharp boundaries.

The strength of the diffuse Nitsche method is the analysis of image-based geometries. The method is able to directly operate on imaging data, completely avoiding the transfer of implicit imaging data into explicit volume and surface parametrizations. At the same time, it reliably delivers the level of accuracy that is required for clinically relevant applications, e.g., for predicting mechanical bone behavior. We therefore believe that the diffuse Nitsche method contributes to a potential pathway for further automating patient-specific simulation, with the eventual goal of establishing evidence-based predictive tools in clinical practice.

Acknowledgments. The Minnesota group gratefully acknowledges support from the National Science Foundation through grants CISE-1565997 and CAREER-1651577. The authors also acknowledge the Minnesota Supercomputing Institute (MSI) of the University of Minnesota for providing computing resources that have contributed to the research results reported within this paper (<https://www.msi.umn.edu/>). The authors are grateful to Thomas Baum and Jan S. Kirschke (Dept. of Neuroradiology, Technische Universität München, Germany) for providing access to the medical imaging data of the vertebra and to Zohar Yosibash (Ben-Gurion-University of the Negev, Beer Sheva, Israel) for helpful comments.

REFERENCES

1. B. Maury. A fat boundary method for the Poisson problem in a domain with holes. *Journal of Scientific Computing*, 16(3):319–339, 2001.
2. A. Bueno-Orovio, V.M. Pérez-García, and F.H. Fenton. Spectral methods for partial differential equations in irregular domains: the spectral smoothed boundary method. *SIAM Journal on Scientific Computing*, 28(3):886–900, 2006.
3. A. Rätz and A. Voigt. PDE’s on surfaces—a diffuse interface approach. *Communications in Mathematical Sciences*, 4(3):575–590, 2006.
4. I. Ramière, P. Angot, and M. Belliard. A fictitious domain approach with spread interface for elliptic problems with general boundary conditions. *Computer Methods in Applied Mechanics and Engineering*, 196:766–781, 2007.
5. X. Li, J. Lowengrub, A. Rätz, and A. Voigt. Solving PDEs in complex geometries: a diffuse domain approach. *Communications in Mathematical Sciences*, 7(1):81, 2009.
6. K.Y. Lervåg and J. Lowengrub. Analysis of the diffuse-domain method for solving PDEs in complex geometries. *arXiv preprint arXiv:1407.7480*, 2014.
7. K.E. Teigen, X. Li, J. Lowengrub, F. Wang, and A. Voigt. A diffuse-interface approach for modeling transport, diffusion and adsorption/desorption of material quantities on a deformable interface. *Communications in Mathematical Sciences*, 4(7):1009, 2009.
8. C.M. Elliott, B. Stinner, V. Styles, and R. Welford. Numerical computation of advection and diffusion on evolving diffuse interfaces. *IMA Journal of Numerical Analysis*, 31(3):786–812, 2011.
9. S. Aland, J. Lowengrub, and A. Voigt. Two-phase flow in complex geometries: A diffuse domain approach. *Computer Modeling in Engineering & Sciences*, 57(1):77, 2010.
10. K.E. Teigen, P. Song, J. Lowengrub, and A. Voigt. A diffuse-interface method for two-phase flows with soluble surfactants. *Journal of Computational Physics*, 230(2):375–393, 2011.
11. C. Miehe, M. Hofacker, and F. Welschinger. A phase field model for rate-independent crack propagation: Robust algorithmic implementation based on operator splits. *Computer Methods in Applied Mechanics and Engineering*, 199(45):2765–2778, 2010.
12. M.J. Borden, C.V. Verhoosel, M.A. Scott, Hughes T.J.R., and C.M. Landis. A phase-field description of dynamic brittle fracture. *Computer Methods in Applied Mechanics and Engineering*, 217–220:77–95, 2012.
13. D. Schillinger, M.J. Borden, and H.K. Stolarski. Isogeometric collocation for phase-field fracture models. *Computer Methods in Applied Mechanics and Engineering*, 284:583–610, 2015.
14. A. Mikelic, M.F. Wheeler, and T. Wick. A phase-field method for propagating fluid-filled fractures coupled to a surrounding porous medium. *SIAM Multiscale Modeling & Simulation*, 13(1):367–398, 2015.
15. M.J. Borden, T.J.R. Hughes, C.M. Landis, A. Anvari, and I.J. Lee. A phase-field formulation for fracture in ductile materials: Finite deformation balance law derivation, plastic degradation, and stress triaxiality effects. *Computer Methods in Applied Mechanics and Engineering*, 312:130–166, 2016.
16. G. Vilanova, I. Colominas, and H. Gomez. Capillary networks in tumor angiogenesis: From discrete endothelial cells to phase-field averaged descriptions via isogeometric analysis. *International Journal for Numerical Methods in Biomedical Engineering*, 29(10):1015–1037, 2013.
17. H. Gomez, L. Cueto-Felgueroso, and R. Juanes. Three-dimensional simulation of unstable gravity-driven infiltration of water into a porous medium. *Journal of Computational Physics*, 238:217–239, 2013.
18. G. Lorenzo, M.A. Scott, K. Tew, T.J.R. Hughes, Y.J. Zhang, L. Liu, G. Vilanova, and H. Gomez. Tissue-scale, personalized modeling and simulation of prostate cancer growth. *Proceedings of the National Academy of Sciences*, page 201615791, 2016.
19. D. Anders, C. Hesch, and K. Weinberg. Computational modeling of phase separation and coarsening in solder alloys. *International Journal of Solids and Structures*, 49(13):1557–1572, 2012.
20. J. Liu, C.M. Landis, H. Gomez, and T.J.R. Hughes. Liquid-vapor phase transition: Thermomechanical theory, entropy stable numerical formulation, and boiling simulations. *Computer Methods in Applied Mechanics and Engineering*, 297:476–553, 2015.
21. Y. Zhao, P. Stein, and B.-X. Xu. Isogeometric analysis of mechanically coupled Cahn-Hilliard phase segregation in hyperelastic electrodes of Li-ion batteries. *Computer Methods in Applied Mechanics and Engineering*, 297:325–347, 2015.
22. S.K.F. Stoter, P. Müller, L. Cicalese, M. Tuveri, D. Schillinger, and T.J.R. Hughes. A diffuse interface method for the Navier–Stokes/Darcy equations: Perfusion profile for a patient-specific human liver based on MRI scans. *Research report* (published online prior to peer review), University of Minnesota, <http://www.tc.umn.edu/~dominik/publications.html>, 2016.
23. L.H. Nguyen, S.K.F. Stoter, T. Baum, J.S. Kirschke, M. Ruess, Z. Yosibash, and D. Schillinger. Phase-field boundary conditions for the voxel finite cell method: surface-free stress analysis of ct-based

- bone structures. *Research report* (published online prior to peer review), University of Minnesota, <http://www.tc.umn.edu/~dominik/publications.html>, 2016.
24. M. Schlottbom. Error analysis of a diffuse interface method for elliptic problems with Dirichlet boundary conditions. *arXiv preprint arXiv:1507.08814v2*, 2016.
 25. F.T.P. Baaijens. A fictitious domain/mortar element method for fluid-structure interaction. *International Journal for Numerical Methods in Fluids*, 35:743–761, 2001.
 26. P. Bastian and C. Engwer. An unfitted finite element method using discontinuous Galerkin. *International Journal for Numerical Methods in Engineering*, 79:1557–1576, 2009.
 27. D. Schillinger, L. Dede’, M.A. Scott, J.A. Evans, M.J. Borden, E. Rank, and T.J.R. Hughes. An isogeometric design-through-analysis methodology based on adaptive hierarchical refinement of NURBS, immersed boundary methods, and T-spline CAD surfaces. *Computer Methods in Applied Mechanics and Engineering*, 249-250:116–150, 2012.
 28. M. Breitenberger, A. Apostolatos, B. Philipp, R. Wüchner, and K.-U. Bletzinger. Analysis in computer aided design: Nonlinear isogeometric b-rep analysis of shell structures. *Computer Methods in Applied Mechanics and Engineering*, 284:401–457, 2015.
 29. E. Burman, S. Claus, P. Hansbo, M.-G. Larson, and A. Massing. CutFEM: discretizing geometry and partial differential equations. *International Journal for Numerical Methods in Engineering*, 104(7):472–501, 2015.
 30. K. Bandara, T. Rüberg, and F. Cirak. Shape optimisation with multiresolution subdivision surfaces and immersed finite elements. *Computer Methods in Applied Mechanics and Engineering*, 300:510–539, 2016.
 31. F. Kummer. Extended discontinuous Galerkin methods for two-phase flows: the spatial discretization. *International Journal for Numerical Methods in Engineering*, doi:10.1002/nme.5288, 2016.
 32. E. Rank, M. Ruess, S. Kollmannsberger, D. Schillinger, and A. Düster. Geometric modeling, isogeometric analysis and the finite cell method. *Computer Methods in Applied Mechanics and Engineering*, 249-250:104–115, 2012.
 33. N. Sukumar, D.L. Chopp, N. Moës, and T. Belytschko. Modeling holes and inclusions by level sets in the extended finite-element method. *Computer Methods in Applied Mechanics and Engineering*, 190:6183–6200, 2001.
 34. G. Legrain, N. Chevaugeon, and K. Dréau. High order X-FEM and levelsets for complex microstructures: uncoupling geometry and approximation. *Computer Methods in Applied Mechanics and Engineering*, 241:172–189, 2012.
 35. M. Mounnassi, S. Belouettar, E. Béchet, S.P.A. Bordas, D. Quoirin, and M. Potier-Ferry. Finite element analysis on implicitly defined domains: An accurate representation based on arbitrary parametric surfaces. *Computer Methods in Applied Mechanics and Engineering*, 200(5):774–796, 2011.
 36. B. Müller, F. Kummer, and M. Oberlack. Highly accurate surface and volume integration on implicit domains by means of moment-fitting. *International Journal for Numerical Methods in Engineering*, 96(8):512–528, 2013.
 37. R.I. Saye. High-order quadrature methods for implicitly defined surfaces and volumes in hyperrectangles. *SIAM Journal on Scientific Computing*, 37(2):993–1019, 2015.
 38. T.-P. Fries and S. Omerovic. Higher-order accurate integration of implicit geometries. *International Journal for Numerical Methods in Engineering*, 106(1):323–371, 2016.
 39. D. Kamensky, M.-C. Hsu, D. Schillinger, J.A. Evans, A. Aggarwal, Y. Bazilevs, M.S. Sacks, and T.J.R. Hughes. An immersogeometric variational framework for fluid–structure interaction: application to bioprosthetic heart valves. *Computer Methods in Applied Mechanics and Engineering*, 284:1005–1053, 2015.
 40. L. Kudela, N. Zander, S. Kollmannsberger, and E. Rank. Smart octrees: Accurately integrating discontinuous functions in 3D. *Computer Methods in Applied Mechanics and Engineering*, page doi:10.1016/j.cma.2016.04.006, 2016.
 41. C. Lehrenfeld. High order unfitted finite element methods on level set domains using isoparametric mappings. *Computer Methods in Applied Mechanics and Engineering*, 300:716–733, 2016.
 42. A. Stavrev, L.H. Nguyen, R. Shen, V. Varduhn, M. Behr, S. Elgeti, and D. Schillinger. Geometrically accurate, efficient, and flexible quadrature techniques for the tetrahedral finite cell method. *Computer Methods in Applied Mechanics and Engineering*, 2016.
 43. J.A. Nitsche. Über ein Variationsprinzip zur Lösung von Dirichlet-Problemen bei Verwendung von Teilräumen, die keinen Randbedingungen unterworfen sind. *Abhandlungen aus dem Mathematischen Seminar der Universität Hamburg*, 36:9–15, 1970.
 44. A. Hansbo and P. Hansbo. An unfitted finite element method, based on Nitsche’s method, for elliptic interface problems. *Computer Methods in Applied Mechanics and Engineering*, 191:537–552, 2002.
 45. M. Ruess, D. Schillinger, Y. Bazilevs, V. Varduhn, and E. Rank. Weakly enforced essential boundary conditions for NURBS-embedded and trimmed NURBS geometries on the basis of the finite cell method. *International Journal for Numerical Methods in Engineering*, 95(10):811–846, 2013.

46. I. Harari and E. Grosu. A unified approach for embedded boundary conditions for fourth-order elliptic problems. *International Journal for Numerical Methods in Engineering*, 104(7):655–675, 2015.
47. B.I. Wohlmuth. A mortar finite element method using dual spaces for the Lagrange multiplier. *SIAM Journal of Numerical Analysis*, 38:989–1012, 2000.
48. A. Gerstenberger and W.A. Wall. An embedded Dirichlet formulation for 3D continua. *International Journal for Numerical Methods in Engineering*, 82:537–563, 2010.
49. M. Griebel and M.A. Schweitzer. A particle-partition of unity method. Part V: boundary conditions. In S. Hildebrandt and H. Karcher, editors, *Geometric Analysis and Nonlinear Partial Differential Equations*, pages 519–542. Springer, 2004.
50. A. Embar, J. Dolbow, and I. Harari. Imposing Dirichlet boundary conditions with Nitsche’s method and spline-based finite elements. *International Journal for Numerical Methods in Engineering*, 83:877–898, 2010.
51. J. Dolbow and I. Harari. An efficient finite element method for embedded interface problems. *International Journal for Numerical Methods in Engineering*, 78:229–252, 2009.
52. C. Annavarapu, M. Hautefeuille, and J.E. Dolbow. A robust Nitsche’s formulation for interface problems. *Computer Methods in Applied Mechanics and Engineering*, 225:44–54, 2012.
53. C. Annavarapu, M. Hautefeuille, and J.E. Dolbow. A Nitsche stabilized finite element method for frictional sliding on embedded interfaces. Part I: single interface. *Computer Methods in Applied Mechanics and Engineering*, 268:417–436, 2014.
54. W. Jiang, C. Annavarapu, J.E. Dolbow, and I. Harari. A robust Nitsche’s formulation for interface problems with spline-based finite elements. *International Journal for Numerical Methods in Engineering*, 104(7):676–696, 2015.
55. A. Düster, J. Parvizian, Z. Yang, and E. Rank. The finite cell method for three-dimensional problems of solid mechanics. *Computer Methods in Applied Mechanics and Engineering*, 197:3768–3782, 2008.
56. D. Schillinger and M. Ruess. The Finite Cell Method: A review in the context of higher-order structural analysis of CAD and image-based geometric models. *Archives of Computational Methods in Engineering*, 22(3):391–455, 2015.
57. Z. Yang, M. Ruess, S. Kollmannsberger, A. Düster, and E. Rank. An efficient integration technique for the voxel-based finite cell method. *International Journal for Numerical Methods in Engineering*, 91:457–471, 2012.
58. D.N. Arnold and W.L. Wendland. Collocation versus Galerkin procedures for boundary integral methods. In *Boundary element methods in engineering*, pages 18–33, 1982.
59. D.N. Arnold, F. Brezzi, B. Cockburn, and D.L. Marini. Unified analysis of discontinuous Galerkin methods for elliptic problems. *SIAM Journal on Numerical Analysis*, 39(5):1749–1779, 2002.
60. B. Cockburn and C.-W. Shu. The local discontinuous Galerkin method for time-dependent convection-diffusion systems. *SIAM Journal on Numerical Analysis*, 35:2440–2463, 1998.
61. E. Burman. A penalty-free nonsymmetric Nitsche-type method for the weak imposition of boundary conditions. *SIAM Journal on Numerical Analysis*, 50(4):1959–1981, 2012.
62. D. Schillinger, I. Harari, M.-C. Hsu, D. Kamensky, K.F.S. Stoter, Y. Yu, and Z. Ying. The non-symmetric Nitsche method for the parameter-free imposition of weak boundary and coupling conditions in immersed finite elements. *Computer Methods in Applied Mechanics and Engineering*, 309:625–652, 2016.
63. Y. Guo, M. Ruess, and D. Schillinger. A parameter-free variational coupling approach for trimmed isogeometric thin shells. *Computational Mechanics*, pages doi:10.1007/s00466-016-1368-x, 2017.
64. F.H. Fenton, E.M. Cherry, A. Karma, and W.-J. Rappel. Modeling wave propagation in realistic heart geometries using the phase-field method. *Chaos: An Interdisciplinary Journal of Nonlinear Science*, 15(1):013502, 2005.
65. M. Ruess, D. Tal, N. Trabelsi, Z. Yosibash, and E. Rank. The finite cell method for bone simulations: Verification and validation. *Biomechanics and Modeling in Mechanobiology*, 11(3):425–437, 2012.
66. A. Quarteroni and A. Valli. *Numerical Approximation of Partial Differential Equations*. Springer, 2008.
67. M. Ruess, D. Schillinger, A.I. Özcan, and E. Rank. Weak coupling for isogeometric analysis of non-matching and trimmed multi-patch geometries. *Computer Methods in Applied Mechanics and Engineering*, 269:46–71, 2014.
68. J.C. Barbosa and T.J.R. Hughes. The finite element method with Lagrange multipliers on the boundary: Circumventing the babuška-brezzi condition. *Computer Methods in Applied Mechanics and Engineering*, 85:109–128, 1991.
69. I. Harari and J. Dolbow. Analysis of an efficient finite element method for embedded interface problems. *Computational Mechanics*, 46:205–211, 2010.
70. R.W. Clough and J. Penzien. *Dynamics of Structures*. McGraw-Hill, 1993.
71. J. Parvizian, A. Düster, and E. Rank. Finite cell method: h - and p - extension for embedded domain methods in solid mechanics. *Computational Mechanics*, 41:122–133, 2007.
72. X. Chen. Generation, propagation, and annihilation of metastable patterns. *Journal of Differential*

- Equations*, 206(2):399–437, 2004.
73. J. Carr and R.L. Pego. Metastable patterns in solutions of $u_t = \varepsilon 2u_{xx} - f(u)$. *Communications on Pure and Applied Mathematics*, 42(5):523–576, 1989.
 74. J. Shen and X. Yang. Numerical approximations of Allen-Cahn and Cahn-Hilliard equations. *Discrete and Continuous Dynamical Systems*, 28(4):1669–1691, 2010.
 75. V. Varduhn, M.-C. Hsu, M. Ruess, and D. Schillinger. The tetrahedral finite cell method: Higher-order immersogeometric analysis on adaptive non-boundary-fitted meshes. *International Journal for Numerical Methods in Engineering*, 107:1054–1079, 2016.
 76. S. Duzcek and U. Gabbert. The finite cell method for polygonal meshes: poly-FCM. *Computational Mechanics*, 58:587–618, 2016.
 77. H. Abels, K.F. Lam, and B. Stinner. Analysis of the diffuse domain approach for a bulk-surface coupled PDE system. *SIAM Journal on Mathematical Analysis*, 47(5):3687–3725, 2015.
 78. M. Burger, O.L. Elvetun, and M. Schlottbom. Analysis of the diffuse domain method for second order elliptic boundary value problems. *Foundations of Computational Mathematics*, pages 1–48, 2015.
 79. V. Nübel. *Die adaptive rp-Methode für elastoplastische Probleme*. Dissertation, Technische Universität München, 2005.
 80. D. Schillinger, J.A. Evans, F. Frischmann, R.R. Hiemstra, M.-C. Hsu, and T.J.R. Hughes. A collocated C^0 finite element method: Reduced quadrature perspective, cost comparison with standard finite elements, and explicit structural dynamics. *International Journal for Numerical Methods in Engineering*, 102(3-4):576–631, 2015.
 81. P.H.F. Nicholson, X.G. Cheng, G. Lowet, S. Boonen, M.W.J. Davie, J. Dequeker, and G. Van der Perre. Structural and material mechanical properties of human vertebral cancellous bone. *Medical Engineering & Physics*, 19(8):729–737, 1997.